MACHINE LEARNING ENHANCED PARAMETRIC REYNOLDS-AVERAGED NAVIER-STOKES EQUATIONS AT THE FULL AND REDUCED ORDER LEVELS

DAVIDE OBERTO^{1,*}, MARIA STRAZZULLO^{2,*} AND STEFANO BERRONE^{2,*}

ABSTRACT. In this contribution, we focus on the Reynolds-Averaged Navier-Stokes (RANS) models and their exploitation to build reliable reduced order models to further accelerate predictions for real-time applications and manyquery scenarios. Specifically, we investigate how machine learning can be employed to enhance the predictive capabilities of the model, both at the Full Order Model (FOM) and Reduced Order Model (ROM) levels. We explore a novel integration of these two areas. We generate the FOM snapshots, essential for ROM construction, using a data-driven RANS model: the ν_t -Vector Basis Neural Network. This is the first time that these machine learning procedure generalizes a large parametric variation, and we propose tailored training strategies to increase the accuracy of the FOM model. At the ROM level, we compare the results obtained by standard Proper Orthogonal Decomposition in an intrusive Galerkin setting (PODG) and POD Neural Network approach (PODNN). The numerical validation is based on a classic turbulent flow benchmark: the flow in a square duct. Our investigation reveals that the PODG method, proves unstable and inaccurate for turbulent flow prediction, while PODNN demonstrates superior performance in terms of accuracy and computational efficiency.

1. Introduction

Reynolds-averaged Navier-Stokes (RANS) equations are a common choice in industry to investigate turbulent flows [25] and they are deduced by formally applying a Reynolds operator to the Navier-Stokes (NS) equations [38]. RANS equations drastically decrease the massive computational cost required for the NS equations simulations based on fine meshes induced by Kolmogorov dissipative scale [36]. However, the application of the Reynolds operator yields a new unclosed tensor term in the RANS equations, the Reynolds Stress Tensor (RST), that needs to be modeled [50] to close the system.

Despite having decades of history, classic RANS models are still inaccurate for some classes of flow due to the poor description of the effects of the RST on the mean flow [4]. Furthermore, they are facing a slow development period, if not even stagnation [29]. Additionally, in spite of the continuous growth of High Performance Computing, scale-resolving models, i.e., models capable of describing the main or

 $E\text{-}mail\ address:\ doberto@sissa.it,\ \{maria.strazzullo,\ stefano.berrone\}@polito.it.\ Date:\ October\ 9.\ 2025.$

¹ Mathlab, Mathematics area, SISSA, Via Bonomea 265, 34136, Trieste, Italy.

 $^{^2}$ Politecnico di Torino, Department of Mathematical Sciences "Giuseppe Luigi Lagrange", Corso Duca degli Abruzzi 24, 10129, Torino, Italy.

^{*} INDAM, GNCS MEMBER.

all the flow features, such as Large-Eddy Simulation (LES) and Direct Numerical Simulation (DNS), are computationally too expensive in industrial settings where tens or hundreds of simulations are required for the same flow typology to perform optimization analysis.

Such motivations have pushed researchers to investigate the use Machine Learning (ML) techniques to define data-driven RANS models, aiming to be computationally cheap as RANS but having an accuracy that is comparable to LES or DNS. Within this framework, the standard setting for ML-based models is to train specific flow configurations using available LES or DNS data [6, 22, 30, 34, 54]. If on one side ML is a valuable asset for enhancing RANS simulations, the generability of these techniques is still limited [23]. This paper is a first step towards a broader parametric model structure where ML-based models can be effectively exploited where a flow configuration changes with respect to a physical parameter (for example the Reynolds number). In this framework, ML-models, once appropriately trained, are suited to generate hundreds of reliable simulations if compared to the high-fidelity data used during the training.

Another important technique when dealing with flows framed in a parametric setting is reduced order modeling (ROM), founded on the offline-online splitting paradigm [37]. In the offline phase, many high-fidelity and computationally expensive full order model (FOM) simulations are performed, spanning a chosen parametric space. Such simulations are generally obtained using classic discretization techniques such as Finite Volume (FV) or Finite Element (FE) methods. From these simulations, usually referred to as snapshots, it is possible to retrieve a parameter-independent basis that spans a low-dimensional space that approximates the full order system. Many methods have been proposed to compute the reduced basis in the literature, and in this paper, we use the Proper Orthogonal Decomposition (POD) [37]. Once the computational expensive offline phase is carried out, in the online phase, for any unseen parameter, an approximate solution belonging to the low-dimensional space is quickly computed in terms of coefficients of the reduced basis expansion.

We investigate the possibility of integrating these two research areas. In particular, we generate the FOM snapshots required by ROM methods using the ν_t -Vector Basis Neural Network (ν_t -VBNN) data-driven RANS models [27], while we use ROM as a real-time tool capable to investigate novel parametric instance in a fast yet accurate way. To the best of the authors' knowledge, while the usage of ROM methods is well established in the computational fluid dynamics community (see, for instance, [12, 14, 15, 45, 55, 56, 59, 60] and the references therein), it is the first time that ML-based RANS and ROMs are leveraged together to generate solutions comparable to the DNS in an affordable computational time.

As a numerical environment to test our procedure, we chose the flow in a square duct. Despite its geometric simplicity, standard eddy-viscosity RANS models fail in the description of the secondary motion that occurs in the cross-square section of the duct, while ML-based RANS models have been proven to achieve DNS-like accuracy for this flow phenomenology [8, 17, 39, 48]. The common setting for training data-driven RANS models is to use data from simulations in the fully turbulent

regime, only. In this work, however, we address the issue of dealing with a wider interval of Reynolds numbers coupling ν_t -VBNN enhanced RANS simulations and the ROM methods, making the model as generalizable as possible in terms of parametric description. In other words, the focus of the data-driven RANS model is not only devoted to accuracy but also to the generalizability over the selected parametric interval.

Once the snapshots for the ROM step are created by the ν_t -VBNN enhanced RANS, we compare an intrusive, i.e., a projection-based model, and a non-intrusive, i.e., purely data-driven, ROM methodology. For the former, we use a POD-Galerkin (PODG) approach that mimics the SIMPLE splitting algorithm proposed at the FOM level, building on [44, 57]. For the latter, we employ the POD Neural Network (PODNN) approach, proposed in [10], to quickly infer the velocity field in the reduced space. This method directly predicts the parameter-dependent coefficients of the POD-based reduced basis expansion, without solving any reduced system.

The main novelties of this contribution are:

- the coverage of both the transitional and fully turbulent regimes by the ML-based RANS model:
- the exploitation of the ML-based RANS snapshots to train ROM models, both intrusive and non-intrusive, to provide a general parametric representation:
- an experimental analysis on the effect of splitting the training data to focus separately on the two flow regimes, both at the full and reduced models.

Besides this introduction, the paper is structured as follows: in Section 2, we briefly recall the closure problem for the RANS equations, present the ν_t -VBNN method and discuss the numerical discretization of the FOM problem; in Section 3, we introduce the ROM aspects that are exploited in this paper; Section 4 focuses on the main characteristics of flow in a square duct, with particular attention to the behavior of the streamwise flow and the secondary motion for different parametric instances; this analysis is preparatory to Section 5, where we describe how the ν_t -VBNN model is used to generate the FOM simulations and the accuracy of the obtained velocity fields is carefully checked; in Section 6 we discuss the ROM results in terms of accuracy and computational time. Finally, in Section 7, conclusions are drawn and possible perspectives discussed.

2. RANS EQUATIONS: CLOSURE AND DISCRETIZATION

This section describes the RANS model we employed to build the reduced surrogate, i.e., the steady RANS model, its discretization, and the ML technique used to enhance its accuracy.

2.1. The Steady RANS equations. The Steady RANS equations are a common choice when dealing with turbulent flows characterized by high Reynolds number $Re = UL/\nu$, being U and L characteristic velocity and length of the flow and ν the kinematic viscosity of the fluid. Considering the domain Ω , Steady RANS equations read as

$$\begin{cases}
\nabla \cdot \boldsymbol{u} = 0, \\
\nabla \cdot (\boldsymbol{u} \otimes \boldsymbol{u}) - \nabla \cdot [2\nu \mathbf{S}] = -\nabla p - \nabla \cdot \boldsymbol{\tau} + \boldsymbol{b},
\end{cases} (1)$$

being: \boldsymbol{u} and p the Reynolds-averaged velocity and pressure fields, respectively, [36, 50], from now on referred as velocity and pressure for the sake of brevity, $\mathbf{S} = \frac{1}{2}[\nabla \boldsymbol{u} + (\nabla \boldsymbol{u})^T]$ the symmetric part of the velocity gradient, $\boldsymbol{\tau} = \boldsymbol{u}' \otimes \boldsymbol{u}'$ the second order symmetric Reynolds stress tensor (RST), with \boldsymbol{u}' the fluctuating component of the velocity and \boldsymbol{b} any force term. We define the Reynolds Force Vector (RFV) as $\boldsymbol{t} = \nabla \cdot \boldsymbol{\tau}$ [5]. Depending to the flow, appropriate boundary conditions should be defined.

In a 3D setting, RANS equations contain ten unknowns and consist of four equations. Thus, some modeling to reduce the number of unknowns is required. To do so, the standard approach consists of writing the RST as a function of some averaged fields, i.e., $\tau = \tau(u, \nabla u, p, \nabla p, \dots)$ either explicitly, through an algebraic relation, or implicitly, as a solution of Partial Differential Equations (PDEs).

Among the algebraic models, we briefly discuss the Eddy-viscosity ones based on Boussinesq's hypothesis

$$\tau = \frac{2}{3}k\mathbf{I} - 2\nu_t \mathbf{S},\tag{2}$$

where $k = \frac{1}{2} \text{tr}(\mathbf{S})$ is the turbulent kinetic energy, ν_t is the turbulent viscosity scalar field, and \mathbf{I} is the identity matrix. Once (2) is inserted into (1), one obtains

$$\begin{cases}
\nabla \cdot \boldsymbol{u} = 0, \\
\nabla \cdot (\boldsymbol{u} \otimes \boldsymbol{u}) - \nabla \cdot [2(\nu + \nu_t)\mathbf{S}] = -\nabla p + \boldsymbol{b},
\end{cases} (3)$$

where, for the sake of brevity, we define the pressure as $p := p + \frac{2}{3}\nabla k$. Equations (3) are still not closed because the turbulent viscosity is unknown.

Several models have been proposed to overcome this issue, such as the Spalart-Allmaras [41], the $k - \omega$ [51] or the $k - \omega$ SST [24] models. In this work, we employ the Launder and Sharma (LS) $k - \varepsilon$ model [19], based on the assumption

$$\nu_t = C_\mu \frac{k^2}{\varsigma},\tag{4}$$

being C_{μ} a known constant, classically $C_{\mu}=0.09$, and ε the dissipation rate of the turbulent kinetic energy. Finally, the model is closed by writing two transport equations for k and ε .

2.2. The ν_t -Vector Basis Neural Network. In this work, we use the ν_t -VBNN as ML model to close and enhance RANS equations. Initially proposed in [1], subsequently improved in [27], and tested in [28], it predicts through two feed-forward neural networks the turbulent viscosity ν_t and the divergence of the orthogonal component of the RST with respect to \mathbf{S} , denoted by $\mathbf{t}^{\perp} = \nabla \cdot (\boldsymbol{\tau} + 2\nu_t \mathbf{S})$.

The idea of predicting an RFV-related field through the data-driven RANS model was proposed in [5] and is justified by the better reliability of the RFV compared to the RST when using DNS results. As a matter of fact, in [47] it is shown that the RFV field retrieved from DNS simulations is less affected by statistical errors compared to the RST because the former can be obtained by first order statistics, namely through \boldsymbol{u} , p and their derivatives. Conversely, the RST tensor is less reliable because second order statistics must be computed.

Furthermore, we predict ν_t and t^{\perp} separately, inspired by [2, 52] to improve the conditioning of the obtained RANS system that, consequently, is less affected by errors induced by the model regression step.

We infer $\tilde{\nu_t} = 1000\nu_t$ and $\tilde{\boldsymbol{t}}^\perp = k^{1/2}/\varepsilon$ \boldsymbol{t}^\perp to handle fields in the order of O(1) or O(10), helping, in this way, the learning procedure [21, 53]. Following [27], $\tilde{\nu_t}$ is predicted by a neural network, while $\tilde{\boldsymbol{t}}^\perp$ is written as linear combinations of a specific vector basis $\{\boldsymbol{v}_k\}_{k=1}^{N_c}$, where the coefficients $\{c_k\}_{k=1}^{N_c}$ of such combination are the targets of the training process. Specifically, we have

$$\tilde{\nu}_t = \nu_t(\lambda_1, \dots, \lambda_{N_i}), \tag{5a}$$

$$\tilde{\boldsymbol{t}}^{\perp} = \sum_{k=1}^{N_c} c_k(\lambda_1, \dots, \lambda_{N_i}) \boldsymbol{v}_k, \tag{5b}$$

where both $\tilde{\nu}_t$ and the coefficients c_k depend on scalar fields λ_i , $i=1,\ldots,N_i$, called *invariants*, obtained by appropriate multiplications of the symmetric and antisymmetric parts of the velocity gradient, i.e., \mathbf{S} and $\mathbf{W} = \frac{1}{2}[\nabla \mathbf{u} - (\nabla \mathbf{u})^T]$, respectively, and ∇k . For a complete list of invariants and of the vector basis, we refer to Appendix A.

In the ν_t -VBNN, the invariants are the inputs of the neural networks, while the outputs are either the turbulent viscosity or the coefficients. This specific setting ensures both Galilean invariance and independence of the chosen frame of coordinates [1, 27]. In practice, to use the ν_t -VBNN model, we first run a RANS simulation with a classic closure model, the LS $k-\varepsilon$ model in our case. Then, we collect the invariants and the vector basis to feed the ν_t -VBNN model. Successively, once $\tilde{\nu_t}$ and \tilde{t}^{\perp} are predicted, the ν_t and t^{\perp} fields are retrieved and inserted into the RANS equations

$$\begin{cases}
\nabla \cdot \boldsymbol{u} = 0, \\
\nabla \cdot (\boldsymbol{u} \otimes \boldsymbol{u}) - \nabla \cdot [2(\nu + \nu_t)\mathbf{S}] = -\nabla p - \boldsymbol{t}^{\perp} + \boldsymbol{b},
\end{cases} (6)$$

to obtain new velocity and pressure fields. We observe that Equation (6) corresponds to (1) with $\nabla \cdot \boldsymbol{\tau} = \boldsymbol{t}^{\perp} - \nabla \cdot [2\nu_t \mathbf{S}]$, that is, a generalization of the Boussinesq's hypothesis in equation (2). In this work, to speed up the online stage, we always set as initial condition of the ν_t -VBNN based simulation the \boldsymbol{u} and p fields obtained by the LS $k-\varepsilon$ model. Moreover, we train the ν_t -VBNN in a parametric setting: the model is trained for different values of the bulk Reynolds number (Re_b) . A more detailed definition of Re_b will follow in Section 4. For now, we anticipate that, in the RANS model, the definition of the Reynolds number can be not trivial and different expressions can be used in the literature for the same flow phenomenology. The Reynolds bulk number is the classical dimensionless quantity used to determine the regime of a flow in a square duct in the literature, i.e., the numerical test we focused on [34, 35]. Once trained, the ν_t -VBNN model is tested for Re_b values not used for training. Both the training stage and the inference stage are schematized in Algorithms 1 and 2, respectively.

2.3. The Finite Volume discretization. In this work, the RANS equations are discretized using the FV method [7, 26] using the OpenFoam library [49]. The FV method deals with the integral form of the differential equations to obtain an algebraic expression in terms of cell-averages. Let us define the computational domain Ω and a tesselation of it (i.e., a mesh), defined as $\mathcal{T} = \{\Omega_i\}_{i=1}^{N_h}$, where $\bigcup_{i=1}^{N_h} \overline{\Omega}_i = \overline{\Omega}$ and $\Omega_i \cap \Omega_j = \emptyset$ for $i \neq j$. Moreover, for the generic field φ , we define

6

Algorithm 1 ν_t -VBNN training

Require: DNS data from N simulations with $\{Re_h^p\}_{p=1}^N$ bulk Reynolds number values, RANS model to improve

Ensure: trained ν_t -VBNN model

1: **for** p = 1, ..., N **do**

Perform RANS simulation with Re_h^p

3:

Compute $\{\lambda_i\}_{i=1}^{N_i}$ and $\{v_j\}_{j=1}^{N_c}$ Interpolate DNS target data on RANS meshes 4:

6: Split data into training and validation set

7: Train for ν_t and \boldsymbol{t}^{\perp} separately

Algorithm 2 ν_t -VBNN inference

Require: Re_b not seen in training stage **Ensure:** ν_t -VBNN-enhanced simulation

1: Run RANS simulation with Re_b ▶ Same RANS model of training stage

2: Compute $\{\lambda_i\}_{i=1}^{N_i}$ and $\{\boldsymbol{v}_j\}_{j=1}^{N_c}$

3: Predict ν_t and \boldsymbol{t}^{\perp} separately with the ν_t -VBNN model

4: Solve for (6) with RANS solution as initial solution and ν_t and t^{\perp} fixed

its cell-average over Ω_i as

$$\varphi_i = \frac{1}{V_i} \int_{\Omega} \varphi \ dV.$$

The integral momentum equation of (3), assuming b = 0, reads:

$$\sum_{i=1}^{N_h} \left[\int_{\Omega_i} \nabla \cdot (\boldsymbol{u} \otimes \boldsymbol{u}) \ dV - \int_{\Omega_i} \nabla \cdot \left[2(\nu + \nu_t) \mathbf{S} \right] \ dV + \int_{\Omega_i} \nabla p \ dV \right] = \mathbf{0}, \quad (7)$$

and, thanks to the Gauss theorem, the volumetric terms containing the divergence operator are recast as surface integrals over the border of the cells. For example,

$$\int_{\Omega_i} \nabla \cdot (\boldsymbol{u} \otimes \boldsymbol{u}) \ dV = \int_{\partial \Omega_i} \boldsymbol{u} \otimes \boldsymbol{u} \cdot d\boldsymbol{S} \approx \sum_f \boldsymbol{S}_f \cdot \boldsymbol{u}_f \ \boldsymbol{u}_f = \sum_f F_f \ \boldsymbol{u}_f, \quad (8)$$

where the summation is over the faces of Ω_i , $S_f = S_f n_f$ is the vector with magnitude equal to the area of the f-th face and direction of its outward normal vector n_f . Finally, u_f is the value of the velocity at the center of the face f. Consequently, F_f is the velocity flux crossing the face f. Analogously, the viscous term reads

$$\int_{\Omega_i} \nabla \cdot \left[2(\nu + \nu_t) \nabla \boldsymbol{u} \right] \, dV = \int_{\partial \Omega_i} 2(\nu + \nu_t) \nabla \boldsymbol{u} \, d\boldsymbol{S} \approx (\nu + \nu_{t_i}) \sum_f (\nabla \boldsymbol{u})_f \cdot \boldsymbol{S}_f.$$

Finally, for the pressure-related term, the pressure gradient is computed using the Gauss theorem:

$$\int_{\Omega_i} \nabla p \ dV = \int_{\partial \Omega_i} p \ d\boldsymbol{S} \approx \sum_f p_f \boldsymbol{S}_f,$$

where p_f in the pressure at the center of the face f.

We highlight that u_f , $(\nabla u)_f$ and p_f are not available in a FV setting and, thus, must be approximated by interpolating the corresponding cell-averaged fields. In this work, all the chosen schemes are second-order accurate, and the used meshes are orthogonal and non-skewed, thus not affecting the order of the discretization of the method [3, 16]. The number of degrees of freedom for the discretized RANS equations through the FV method is $N_h^u = 3N_h$ for the velocity field and $N_h^p = N_h$ for the pressure field.

2.4. **The SIMPLE algorithm.** The discretized RANS equations can be written in matrix form as

$$\begin{pmatrix} \mathbf{A}_h(\boldsymbol{u}_h) & G_h \\ M_h & 0 \end{pmatrix} \begin{pmatrix} \boldsymbol{u}_h \\ p_h \end{pmatrix} = \begin{pmatrix} \boldsymbol{b}_h \\ 0 \end{pmatrix}, \tag{9}$$

where the matrix $\mathbf{A}_h(\boldsymbol{u}_h) \in \mathbb{R}^{N_h^{\boldsymbol{u}} \times N_h^{\boldsymbol{u}}}$ is associated to the discretization of the diffusive and convective terms of the RANS equations, $G_h \in \mathbb{R}^{N_h^{\boldsymbol{u}} \times N_h^p}$ is the discretized pressure operator, $M_h \in \mathbb{R}^{N_h^p \times N_h^{\boldsymbol{u}}}$ is the discretized divergence operator, and $\boldsymbol{b}_h \in \mathbb{R}^{N_h^{\boldsymbol{u}}}$ represents any source term. Instead of dealing with the fully coupled system (9), we exploit the Semi-Implicit Method for Pressure-Linked Equations (SIMPLE) algorithm [32] to decouple the ν_t -VBNN RANS system using an iterative strategy.

Let us assume that the target velocity field can be written as $u_h = u_h^* + u_h'$, where u^* plays the role of a velocity predictor, that is not divergence-free, and u_h' is interpreted as a correction to enforce the divergence-free condition. In addition, the pressure field is written as $p_h = p_h^* + p_h'$, where p_h^* is the pressure value at the previous iteration. Finally, given the parameter instance Re_b , let us denote by ν_t and t^{\perp} the turbulent fields obtained by the ν_t -VBNN model. Then, the (k+1)-th step of the SIMPLE algorithm for RANS equations can be schematized as follows:

i) the matrix $\mathbf{A}_h = \mathbf{A}_h(\boldsymbol{u}_h^k)$ is split as sum of its diagonal part \mathbf{D}_h and its extra-diagonal part \mathbf{H}_h , i.e., $\mathbf{A}_h = \mathbf{D}_h + \mathbf{H}_h$. We remark that \mathbf{A}_h depends on ν_t . The discrete velocity predictor \boldsymbol{u}_h^* is retrieved by solving

$$\left(\mathbf{H}_h + \frac{1}{\alpha_u} \mathbf{D}_h\right) \mathbf{u}_h^* = -G_h p_h^k + \mathbf{b}_h + \left(\frac{1}{\alpha_u} - 1\right) \mathbf{D}_h \mathbf{u}_h^k, \tag{10}$$

where $\alpha_{\boldsymbol{u}} \in (0,1]$, called under-relaxation factor, is usually kept fixed for all iterations and increases the diagonal dominance of the system. We remark that in (10), \boldsymbol{b}_h depends on \boldsymbol{t}^{\perp} ;

- ii) all fluxes are computed at the cell boundaries using \boldsymbol{u}_h^* and the discrete operators are updated;
- iii) assuming $\mathbf{H}_h u_h' = \mathbf{0}$, we deduce that the velocity correction reads

$$\mathbf{u}_h' = -\mathbf{D}_h^{-1} G_h p_h'. \tag{11}$$

To obtain the pressure correction p'_h to enforce the diverge-free condition $M_h \mathbf{u}_h = M_h (\mathbf{u}_h^* + \mathbf{u}_h') = 0$, the following Poisson equation is solved

$$-M_h(\mathbf{D}_h^{-1}G_hp_h') = -M_h\mathbf{u}_h^*; \tag{12}$$

- iv) we define $p^{k+1} = p_h^k + \alpha_p p_h'$, being $\alpha_p \in (0,1]$ the under-relaxation factor for the pressure field defined to increase the stability of the method;
- v) exploiting (11), the new velocity is

$$\mathbf{u}_{h}^{k+1} = \mathbf{u}_{h}^{*} - \mathbf{D}_{h}^{-1} G_{h} \mathbf{p}_{h}'. \tag{13}$$

Algorithm 3 synthesizes the SIMPLE algorithm given some stopping criteria sc, usually based on the residual of system and/or on the rate of change of the obtained velocity and pressure fields compared to the previous ones.

Algorithm 3 The SIMPLE algorithm

```
Require: \boldsymbol{u}_h^0 and p_h^0, Re_b, \alpha_{\boldsymbol{u}}, \alpha_p, number max of iterations N_{max}, sc

Ensure: discrete solutions \boldsymbol{u}_h, p_h

1: k=0

2: \nu_t, \boldsymbol{t}^\perp \leftarrow \nu_t-VBNN(Re_b), see Algorithm 2

3: while not sc and k \leq N_{max} do

4: u_h^* \leftarrow Solve (10) for the velocity predictor using p_h^k

5: Obtain through interpolation the fluxes fields using \boldsymbol{u}_h^*

6: p_h' \leftarrow Solve (12) with \boldsymbol{u}_h^* and updated fluxes

7: p_h^{k+1} = p^k + \alpha_p p_h'

8: \boldsymbol{u}_h^{k+1} \leftarrow Correct the velocity using (13)

9: k \leftarrow k+1

10: end while

11: Return \boldsymbol{u}_h = \boldsymbol{u}_h^k, p_h = p_h^k
```

3. Reduced order modeling for RANS Equations

This section focuses on the ROM application to the proposed ν_t -VBNN RANS model. First, we describe the POD approach, which is employed to build the low-dimensional framework. Next, we briefly discuss the two algorithms we are going to compare in the numerical results, i.e., the PODNN [10] and the PODG SIMPLE [57].

3.1. The POD approach. ROM techniques aim to create a surrogate model building on some high-fidelity information, i.e., FOM simulations. The core idea behind ROM is to initially invest computational effort in generating a low-dimensional model derived from FOM solutions. Despite its significantly reduced size, the system is still accurate and can be effectively and efficiently used to explore a wide range of parametric scenarios. At the FOM level, we obtain the solutions by means of a trained ν_t -VBNN RANS discretized through FV. Namely, we take N_s snapshots of ν_t -VBNN RANS simulations, for several Re_b in the considered parametric range, denoted as \mathcal{P} , i.e., we consider $\{u_h(Re_b^i)\}_{i=1}^{N_s}$ and $\{p_h(Re_b^i)\}_{i=1}^{N_s}$, for $Re_b^i \in \mathcal{P}$. For details on the POD algorithm, we refer to [11, 37]. The POD yields a set of basis functions $\{\varphi_j\}_{j=1}^{r_u}$ and $\{\psi_j\}_{j=1}^{r_p}$, for velocity and pressure, respectively. The reduced spaces spanned by these two sets of basis functions are \mathbb{U}_r and \mathbb{Q}_r , and we write

$$\mathbb{U}_r = \operatorname{POD}(\{\boldsymbol{u}_h(Re_b^k)\}_{k=1}^{N_s}, r) \quad \text{and} \quad \mathbb{Q}_r = \operatorname{POD}(\{p_h(Re_b^k)\}_{k=1}^{N_s}, r),$$

assuming for the sake of presentation that $r_u = r_p = r$. In the reduced setting, $\mathbf{u}_r(x, Re_b) = \mathbf{u}_r \in \mathbb{U}_r$ and $p_r(x, Re_b) = p_r \in \mathbb{Q}_r$ represent the reduced velocity and pressure fields, respectively, and they can be expanded as

$$\mathbf{u}_r = \sum_{j=1}^r a_j(Re_b)\boldsymbol{\varphi}_j(x)$$
 and $p_r = \sum_{j=1}^r b_j(Re_b)\psi_j(x)$,

for some reduced real coefficients $\{a_j(Re_b)\}_{j=1}^r$ and $\{b_j(Re_b)\}_{j=1}^r$, respectively. The vectors in \mathbb{R}^r , whose entries are defined by the reduced coefficients, are denoted by a and b, for velocity and pressure. Finally, we define $\mathbf{U}_r \in \mathbb{R}^{N_h^u \times r}$ and $Q_r \in \mathbb{R}^{N_h^p \times r}$ as the two matrices gathering as columns the reduced basis vector for the velocity and pressure field, respectively.

3.2. **PODNN method for RANS Equations.** Recently, thanks to the gain of popularity of ML and the increasing data-availability in computational sciences, pure data-driven approaches have been exploited. In this work, we use the PODNN [10] as a non-intrusive approach. This method approximates the maps between the parameter space and the reduced coefficients through feed-forward neural networks. In our setting, the two approximated maps are

$$\pi_{\boldsymbol{u}}: Re_b \mapsto a$$
 and $\pi_p: Re_b \mapsto b$.

Once the PODNN model is properly trained, the online phase consists of making inferences of the neural networks, completely disregarding the nature of the underlying physical model and avoiding all issues associated to nonlinear terms in the PDEs.

The reduced coefficients required for the training of the neural networks can be retrieved from the FOM snapshots by solving the following normal systems [33]

$$\mathbf{U}_r^T \mathbf{X}_h \mathbf{U}_r a(Re_h^k) = \mathbf{U}_r^T \mathbf{X}_h \mathbf{u}_h(Re_h^k), \tag{14a}$$

$$Q_r^T X_h Q_r b(Re_b^k) = Q_r^T X_h p_h(Re_b^k), \tag{14b}$$

for $k=1,\ldots,N_s$, where $\mathbf{X}_h \in \mathbb{R}^{N_h^u \times N_h^u}$ and $X_h \in \mathbb{R}^{N_h^p \times N_h^p}$ are symmetric positive definite matrices. In particular, in our work X_h is the L^2 -norm inducing matrix, i.e. the diagonal matrix having as i-th diagonal component the cell volume V_i , while \mathbf{X}_h is the diagonal matrix having on the diagonal the same diagonal of X_h repeated three times.

3.3. PODG SIMPLE method for RANS Equations. A classic approach to obtain the reduced coefficients is to solve the reduced system deduced by Galerkin-projection of some full-order linear systems [37]. Several studies highlight the benefits of using consistent models at the FOM and ROM level [13, 46], and, thus, we adopt an iterative algorithm that mimics the full order SIMPLE strategy at the reduced level [55, 56], referred to as PODG SIMPLE.

Given an initial guess on the reduced coefficients vectors a^0 and b^0 , the PODG SIMPLE algorithm follows the same steps of the SIMPLE algorithm by iteratively solving a linear system for the velocity predictor, followed by one for the pressure correction. In particular, the reduced velocity predictor equation reads

$$\mathbf{U}_r^T \left(\mathbf{H}_h + \frac{1}{\alpha_u} \mathbf{D}_h \right) \mathbf{U}_r a^* = \mathbf{U}_r^T \left[-G_h Q_r b^k + \boldsymbol{b}_h + \left(\frac{1}{\alpha_u} - 1 \right) \mathbf{D}_h \mathbf{U}_r a^k \right], \quad (15)$$

where a^* denotes the reduced coefficients of the velocity predictor, while the equation for the reduced coefficients of the pressure correction reads

$$-Q_r^T M_h(\mathbf{D}_h^{-1} G_h Q_r b') = -Q_r^T M_h \mathbf{U}_r a^*. \tag{16}$$

Remark 1. One could use different under-relaxation factors in the reduced model and the full order one. In this work, to mimic as much as possible the FOM framework, we use the same relaxation factors for the FOM and ROM.

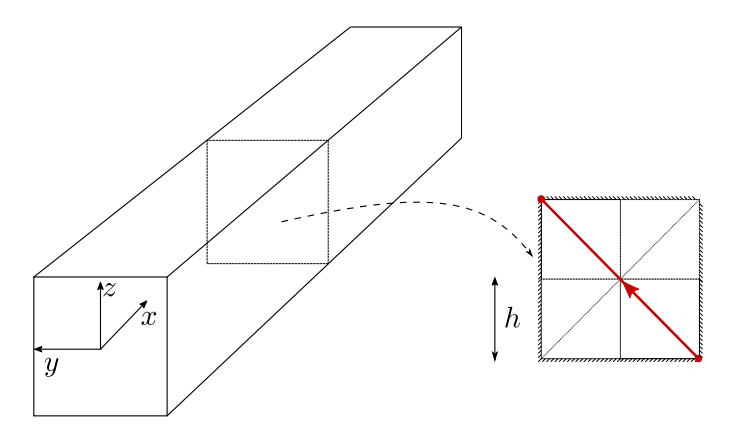


FIGURE 1. Square duct geometry.

Remark 2. To assemble the \mathbf{H}_h and \mathbf{D}_h matrices and the \mathbf{b}_h vector, one should take into account the turbulent fields ν_t and \mathbf{t}^{\perp} . In the numerical results, we opt for using the same turbulent fields of the FOM model. Namely, for each new parameter instance, the ν_t -VBNN approach is used and, consequently, the FOM matrices are assembled. The rationale behind this choice relies on comparing the most consistent projection-based ROM model to the non-intrusive PODNN strategy. We anticipate that even this consistent choice will lead to poor velocity field approximations.

The whole PODG SIMPLE algorithm is presented in Algorithm 4.

```
Algorithm 4 The PODG SIMPLE algorithm
```

```
Require: a^0 and b^0, \mathbf{U}_r and Q_r, Re_b, \alpha_u, \alpha_p, N_{max}, sc
Ensure: reduced coefficients a, b
 1: k = 0
 2: \nu_t, \boldsymbol{t}^{\perp} \leftarrow \nu_t-VBNN(Re_b)
 3: while not sc and k \leq N_{max} do
         a^* \leftarrow \text{Solve (15)} for the velocity predictor using b^k
         Obtain through interpolation the fluxes fields using a^*
 5:
         b' \leftarrow \text{Solve (16)} with a^* and updated fluxes
 6:
         b^{k+1} = b^k + \alpha_n b'
 7:
         a^{k+1} \leftarrow \text{Correct the velocity using } b'
 8:
         k \leftarrow k+1
10: end while
11: Return a = a^k, b = b^k
```

4. The Duct Flow Benchmark

In this section, we provide the essential insights on the phenomenology of the flow in a square duct to better analyse the FOM and ROM results in the next sections.

4.1. Flow phenomenology. The flow in a square duct is a classic benchmark in the turbulence modeling community [22]. DNS data from Pinelli et al. [34] are

available for several bulk Reynolds numbers $Re_b = U_b \ h/\nu$, being U_b the mean cross-section velocity and h half duct width, see Figure 1. Periodic boundary conditions are imposed at the inlet-outlet faces while classic no-slip boundary conditions at wall are set. The U_b value is imposed by applying the appropriate b value in (1). This flow is statistically uniform in the streamwise-direction and, thus, time-averaged velocity and Reynolds stresses on a cross-section only are provided in [34]. Moreover, it exhibits a secondary motion, associated with non-negligible u_y and u_z components. We define its intensity as

$$I_s = \sqrt{u_y^2 + u_z^2}/U_b.$$

This flow is of great interest for turbulence modeling because classic eddy-viscosity models, such as the LS $k-\varepsilon$ model used in this work, systematically fail in the secondary motion prediction [21, 53], see Appendix B for a deeper analysis.

Pinelli et al. dataset consists of sixteen simulations with Re_b ranging from 1100 to 3500. We decided to discard the $Re_b \in \{1100, 1150, 1250\}$ results because we observed that the averaged velocity fields were affected by strong asymmetry for the cross-section symmetries, possibly due to the choice of a not wide enough timespan averaging when computing statistics. A possible solution would have been to average the DNS data across the cross-section symmetry axes as proposed in [8]. However, we opted to deal with asymmetric fields to test the robustness of our model to unavoidable statistical and numerical errors coming from DNS data from generic simulations.

The flow behavior changes significantly in the investigated Re_b interval. For lower Reynolds numbers, the flow is in a transitional regime from laminar to turbulent, while for higher Re_b values, the flow is fully turbulent. Pinelli et al. identified $Re_b = 2000$ as the threshold value of these two distinct regimes. The flow phenomenology depending on Re_b can be observed by looking at I_s in Figure 2. It immediately appears that, at lower Re_b regimes, secondary motion occurs not only near the corners but also near the walls' midpoints, contrary to the high Reynolds regime. In addition, the behavior of I_s along the diagonals changes with respect to the Re_b value. In particular, Figure 3 shows I_s along the red cross-section diagonal displayed in Figure 1. For the low Re_b regime, depicted in Figure 3a, the I_s maxima significantly increases with respect to Re_b , while it is not the case for $Re_b > 2000$ where a marginal opposite trend can be observed. Finally, independently of the flow regime, the higher Re_b , the closer the maxima of I_s are to the corners.

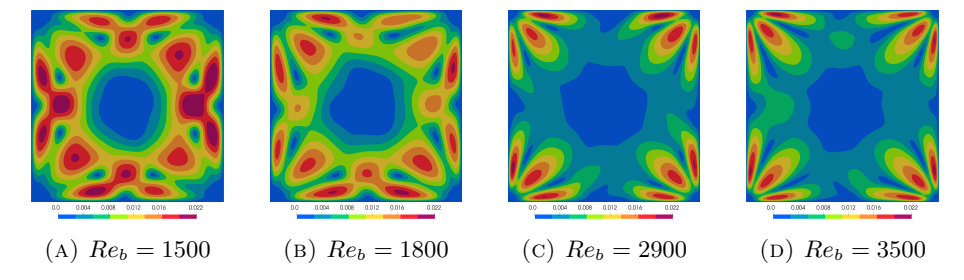


FIGURE 2. I_s for the flow in a square duct for different Re_b . The results come from the Pinelli et al. dataset [34].

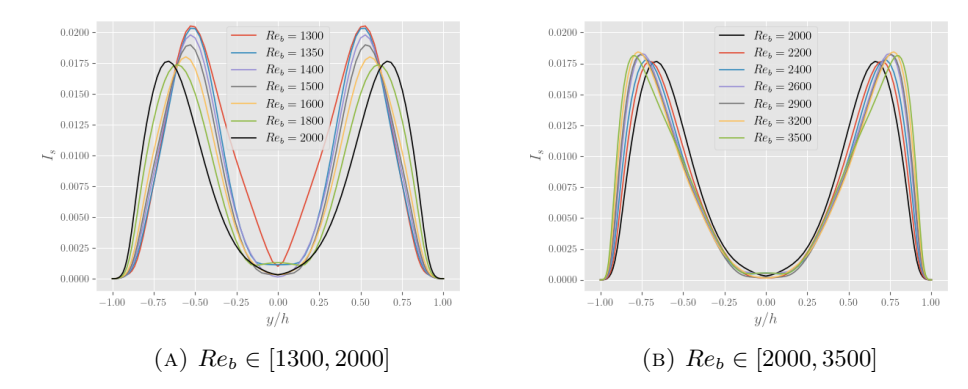


FIGURE 3. I_s over the red diagonal represented in Figure 1 for different Re_b ranges: low and turbulent regimes in the left and right plot, respectively.

TABLE 1. Three different networks training settings. Re_b interval indicates the Re_b range used, # simulations specifies how many simulations have been used for training, Re_b kept out reports the Re_b value(s) kept out from training.

	Re_b interval	# simulations	Re_b kept out
all	[1300, 3500]	11	1600, 2900
low	[1300, 2000]	6	1600
high	[2000, 3500]	6	2900

5. FOM RESULTS

In this Section, we train the ν_t -VBNN model to enhance the accuracy of RANS equations to generate FOM results for several values of Re_b .

5.1. ν_t -VBNN training. First, the neural networks of the ν_t -VBNN model to predict $\tilde{\nu}_t$ and $\tilde{\mathbf{t}}^{\perp}$ must be trained. We perform it on a wider Re_b range compared to the majority of works dealing with the square duct case [1, 5, 52, 53]. Indeed, we select Re_b ranging from 1300 to 3500, for a total of thirteen simulations. The reason is twofold: on one hand, our model will be used to generate around one hundred of FOM simulations to build an effective ROM that should be able to span a significantly large parameter space; on the other hand, by covering two different and distinct flow regimes, we make the investigated problem more challenging. To access the effect of dealing with two flow regimes, we train, for both $\tilde{\nu}_t$ and $\tilde{\mathbf{t}}^{\perp}$, three different neural networks with data coming from different Re_b values: one with $Re_b \in [1300, 3500]$, one with $Re_b \in [1300, 2000]$ and one with $Re_b \in [2000, 3500]$, referred as all, low, and high, respectively. For each case, data from at least one DNS simulation is kept out from training to test our network's ability on unseen data. Table 1 summarizes all this information.

All models are implemented using the pyTorch python library [31]. Regarding

Table 2. Selected λ_{ν_t} and $\lambda_{\tilde{t}^{\perp}}$ values for the all, low and high models.

	all	low	high
$\lambda_{ ilde{ u}_t}$	10^{-3}	10^{-3}	10^{-4}
$\lambda_{ ilde{m{t}}^{\perp}}$	10^{-4}	10^{-4}	10^{-5}

the optimization procedure, the $\tilde{\nu}_t$ and \tilde{t}^{\perp} networks are trained using the Adam algorithm [18] to minimize the following discretized loss functions, respectively:

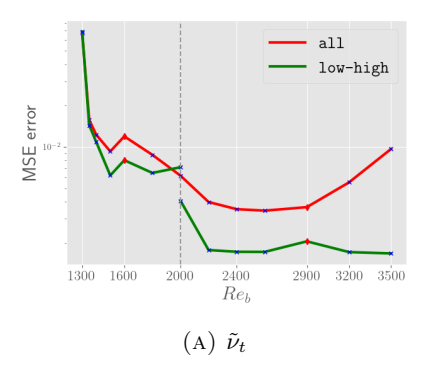
$$\mathcal{L}_{\tilde{\nu}_t}(\cdot; \theta_{\tilde{\nu}_t}) = \frac{1}{n} \sum_{i=1}^n (\tilde{\nu}_{t,i}^{\text{DNS}} - \tilde{\nu}_{t,i}^{\text{NN}}(\cdot))^2 + \lambda_{\tilde{\nu}_t} \sum_{i=1}^{n_{\tilde{\nu}_t}} (\theta_{\tilde{\nu}_t}^i)^2, \tag{17a}$$

$$\mathcal{L}_{\tilde{t}^{\perp}}(\cdot; \theta_{\tilde{t}^{\perp}}) = \frac{1}{3n} \sum_{i=1}^{n} \sum_{j=1}^{3} (\tilde{t}_{j,i}^{\perp, \text{DNS}} - \tilde{t}_{j,i}^{\perp, \text{NN}}(\cdot))^{2} + \lambda_{\tilde{t}^{\perp}} \sum_{i=1}^{n_{\tilde{t}^{\perp}}} (\theta_{\tilde{t}^{\perp}}^{i})^{2}, \tag{17b}$$

where we denote by $\tilde{\nu}_t^{\mathrm{DNS}}$ and $\tilde{t}^{\perp,\mathrm{DNS}}$ the discrete DNS target fields interpolated on the RANS mesh, by $\tilde{\nu}_t^{\mathrm{NN}}$, and $\tilde{t}^{\perp,\mathrm{NN}}$ the fields predicted thought neural networks using (5), by $\theta_{\tilde{\nu}_t} \in \mathbb{R}^{n_{\tilde{\nu}_t}}$ and $\theta_{\tilde{t}^{\perp}} \in \mathbb{R}^{n_{\tilde{t}^{\perp}}}$ the vectors containing the weights of the neural networks to be tuned in the optimization procedure, by $\lambda_{\tilde{\nu}_t}$ and $\lambda_{\tilde{t}^{\perp}}$ the so-called regularization factors. By the pedex i, we denote the i-th element of the discretized field or the i-th weight of the network, while j spans the three components of \tilde{t}^{\perp} .

For each network and each hyperparametric choice, fifteen training runs with different randomly sampled starting weights are performed. For each Re_b value used to train, we extract the fields required for the ν_t -VBNN training from the N_h computational cells of the RANS simulation. The 80% of these data are used to train the networks, while the remaining 20% are used for validation purposes during the training.

During the hyperparameters tuning stage, we observed a strong dependence of the overfitting behavior of the ν_t -VBNN model from the regularization factors. Consequently, we rigorously carried out an analysis to find their optimal values in terms of testing errors. The results are detailed in Appendix C. The final choices for the regularization parameters are reported in Table 2, while additional information about the networks' architecture are presented in Appendix D. It appears that a smaller regularization parameter can be used when training on a unique flow regime without occurring in overfitting. This behavior can be intuitively explained as follows: when inferring with a new Re_b value belonging to the same flow regime as all the training Re_b values, the expected $\tilde{\nu}_t$ and \tilde{t}^{\perp} fields are close to all training fields, thus reducing the overfitting phenomenon. Finally, each training is stopped if the minimum of the validation loss does not decrease for fifty consecutive epochs for a maximum of $N_e = 500$ epochs. Generally speaking, the average training time per epoch for the all networks is the double of the low and high one, being the former around 60s and the latter around 30s. This behavior is due to the all networks being trained with the double of data compared to the low and high networks.



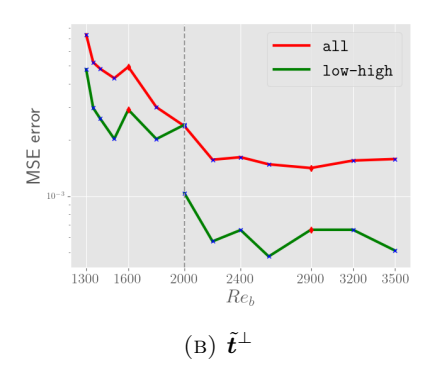


FIGURE 4. MSE with respect to Re_b for the chosen NNs. The simulations used and discarded in the training are denoted by blue stars and red diamonds, respectively.

To emphasize the benefits of splitting the ν_t -VBNN models training into the low and high intervals, Figure 4 shows the MSE of the inferred fields with respect to Re_b for the final selected networks. It immediately appears that the training interval splitting approach leads to lower errors because each neural network focuses on a specific flow regime. In the following, we will refer to the setting with ν_t -VBNN neural networks trained using data from $Re_b \in [1300, 3500]$ as all, while to the setting with separate trainings depending on the Re_b value as low-high. In the latter, the low network is selected for inference if $Re_b < 2000$, otherwise the high one is used.

5.2. **FOM results.** Once the models for both the all and low-high settings are trained, the ν_t -VBNN enhanced simulations can be performed to generate high-fidelity FOM simulations avoiding the computational burden of DNS.

To access the FOM accuracy, Figures 5 and 6 show both the streamwise velocity u_x/U_b and the intensity of the secondary motion I_s for $Re_b=1600$ and $Re_b=2900$. Data from these Re_b values were kept out during training for both all and low-high models. The larger discrepancies between the all and low-high settings are observable for the $Re_b=1600$ case, where the former poorly represents the maximum isocontours shape of the streamwise velocity and underestimates I_s , while the latter systematically better predicts both fields. Conversely, discrepancies between the two settings for $Re_b=2900$ are less prominent, but noticeable, especially for the I_s field. Also for this case, the low-high model gives closer results to DNS.

To give a quantitative measure of the all and low-high accuracy, Figure 7 depicts the maximum values of I_s along the cross-section diagonal while varying Re_b and compares them to the DNS values (i.e., the maxima of curves in Figure 3). For clarity, the values are divided into two plots, one for each flow regime. Regarding the $Re_b \in [1300, 2000]$ regime, neither setting can predict the decreasing trend of the maxima. However, the low-high setting predicts maxima closer to DNS compared to the all one. Regarding the $Re_b \in [2000, 3500]$ regime, the low-high and all maxima values are close except for the lowest Re_b values where the all setting drastically underestimates the maxima, while the low-high one overestimates them.

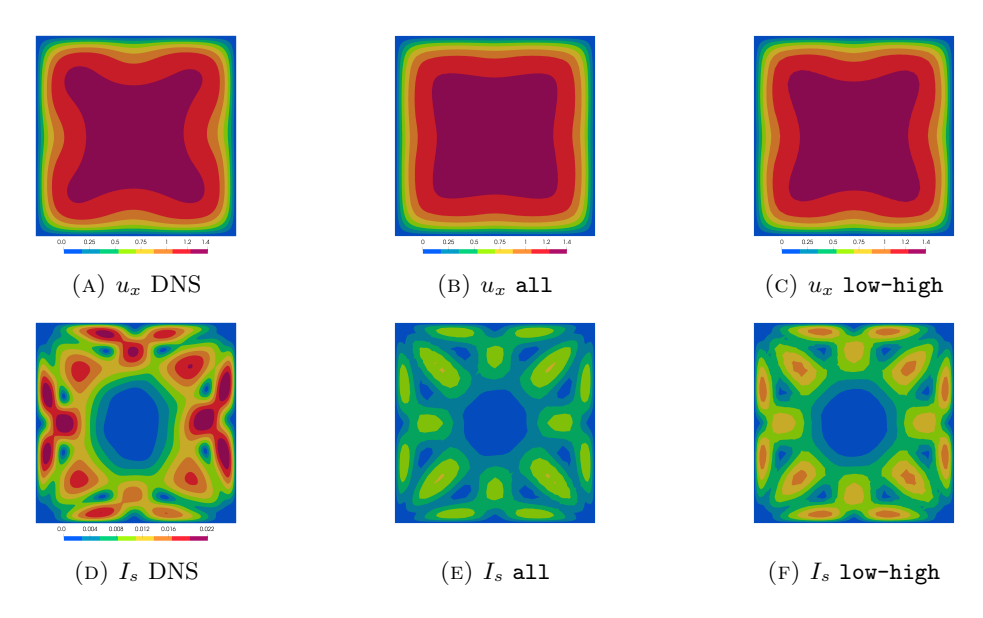


FIGURE 5. Comparison of u_x/U_b and I_s obtained with the all and low-high models at $Re_b=1600$ and the DNS references.

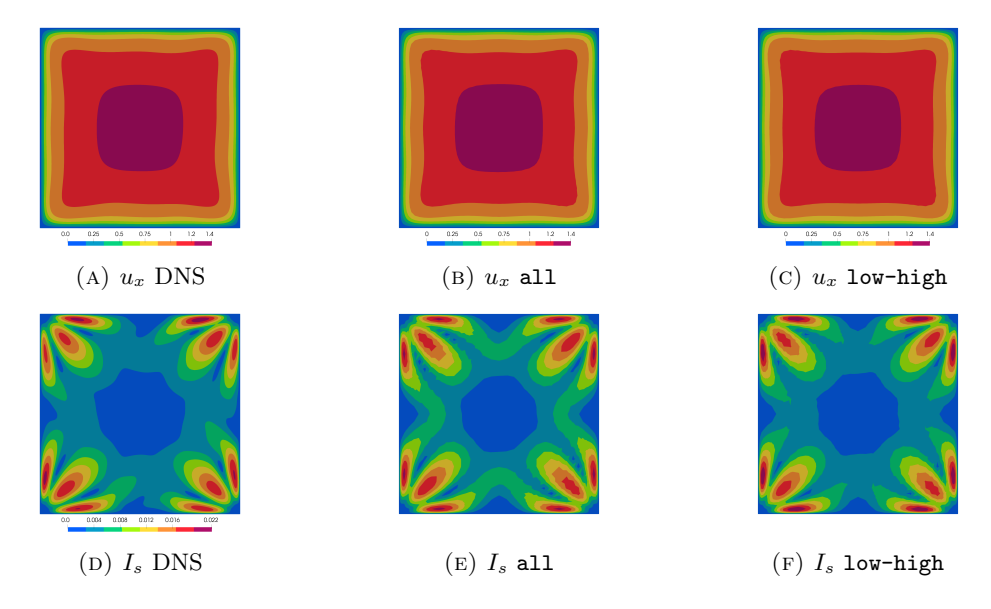


FIGURE 6. Comparison of u_x/U_b and I_s obtained with the all and low-high models at $Re_b=2900$ and the DNS references.

Furthermore, Figure 8 shows the location of the maxima in terms of the positive coordinate y/h. For both flow regimes, either the maxima locations of the two models coincide, or the low-high maxima are closer to DNS. Finally, we highlight

that for $Re_b = 2900$ the maximum values of I_s are close and their locations are identical for the two settings, in agreement with Figure 6.

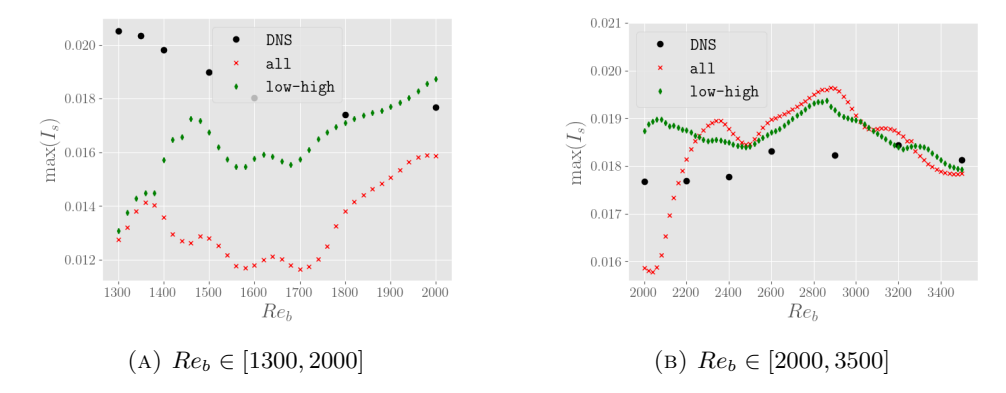


FIGURE 7. Maximum values of I_s along the square section diagonal with respect to Re_b . The all and low-high values are compared to DNS.

Moreover, Figure 9 shows the relative L^2 error of the two models for the velocity field prediction using DNS data as reference. The low-high model systematically outperforms the all one both for Re_b training values and for testing values. Summarizing, the low-high model is more accurate than the all model, in terms of prediction of the streamwise velocity and secondary motion, both quantitatively and qualitatively. For this reason, we decided to use the low-high model to build the ROM space.

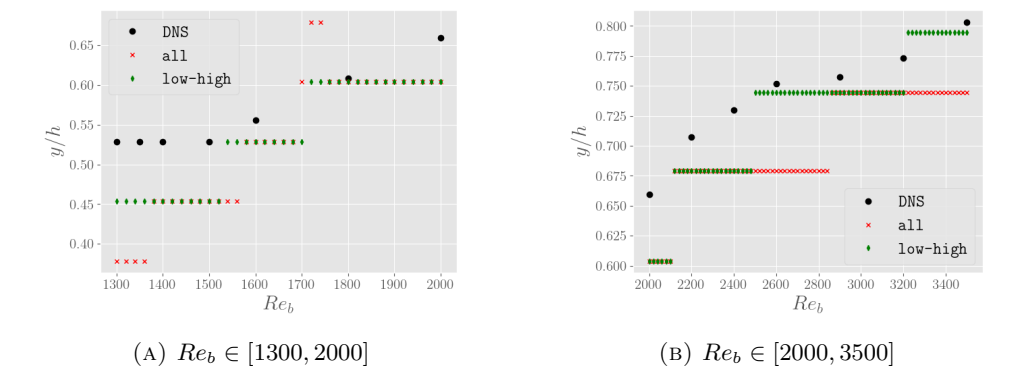


FIGURE 8. y/h location of the maximum value of I_s along the upper part (y/h>0) square section diagonal with respect to Re_b . The all and low-high values are compared to the DNS ones.

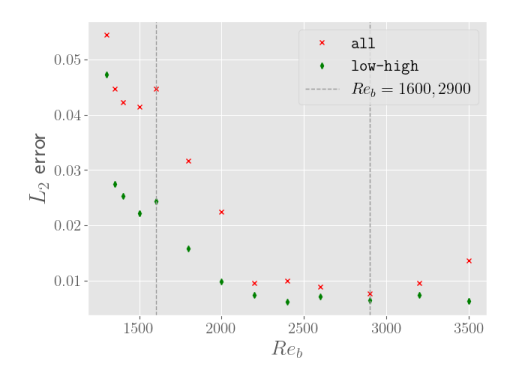


FIGURE 9. Relative L^2 error in the velocity prediction for the all and low-high models using DNS data as reference.

6. ROM results

This section analyses the results of both the PODG SIMPLE and PODNN approaches in the flow in a square duct setting. To create the reduced models, we use the low-high high-fidelity ν_t -VBNN enhanced simulations as snapshots.

6.1. Reduced space construction. We generate simulations for

$$Re_b \in \{1300, 1320, \cdots, 3480, 3500\},\$$

removing the Re_b values contained in the DNS datasets, as snapshots for the POD method. To perform a consistent analysis with respect to the previous section, we investigate the possibility of splitting the Re_b interval into two sub-intervals corresponding to the two flow regimes with $Re_b = 2000$ as the threshold value. Thus, we define the all-POD approach, with the reduced basis generated using all snapshots, the low-POD approach, using the $Re_b < 2000$ snapshots, and the high-POD approach, using the $Re_b > 2000$ snapshots. In particular, we have $N_s = 99$ for the all-POD, $N_s = 30$ for the low-POD, and $N_s = 69$ for the high-POD.

Given the positive eigenvalues $\{\lambda_i\}_{i=1}^{N_s}$ of a snapshot covariance matrix, sorted in decreasing order, we select the number of kept modes r_u and r_p , for velocity and pressure respectively, for each approach as the smallest $i \in \mathbb{N}$ value such that $\sum_{j=i}^{N_s} \lambda_j / \sum_{j=1}^{N_s} \lambda_j < 10^{-7}$. We remark that with $\{\lambda_i\}_{i=1}^{N_s}$, we can refer to velocity or pressure eigenvalues depending on the context. We obtain $r_u = 22$ and $r_p = 29$, $r_u = 14$ and $r_p = 24$ and $r_u = 13$ and $r_p = 22$ for the all-, low- and high-POD approaches respectively. The all-POD requires higher r_u and r_p values to retain the same energy of the other approaches due to the wider phenomenology covered by the snapshots. For completeness, in Figure 10, we show the eigenvalues' decays (green for velocity and red for pressure).

6.2. **PODNN training.** Depending on the selected reduced basis, the PODNN is trained targeting as outputs the reduced coefficients retrieved from the FOM snapshots using (14). When investigating the flow in a square duct, especially in the data-driven RANS turbulence community, the results analysis is restricted on the velocity field only [1, 52, 53]. Consequently, we train a PODNN for the prediction of the velocity reduced coefficients only, disregarding the pressure contribution. This approach is possible thanks to the non-intrusive nature of the PODNN method

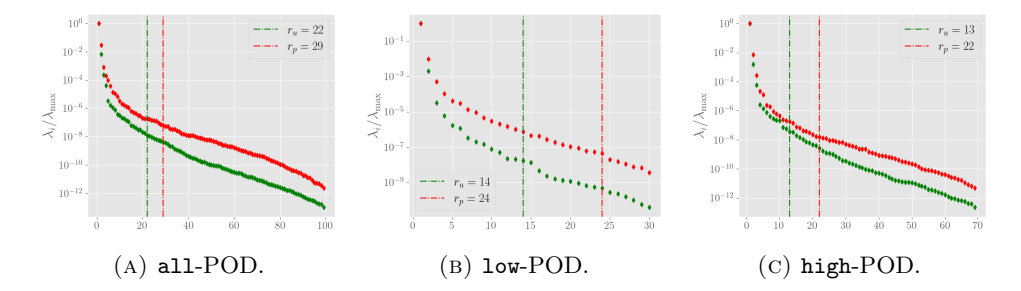


FIGURE 10. Normalized eigenvalues $\lambda_i/\lambda_{\text{max}}$ of the covariance matrices (green and red for velocity and pressure, respectively).

that is not affected by the intrinsic coupling between velocity and pressure given by the RANS equations. Two models are defined: one to predict the velocity reduced coefficients associated to the all-POD basis and one to predict, through two neural networks, the velocity reduced coefficients associated to the low-POD and high-POD basis, depending if $Re_b < 2000$ or $Re_b > 2000$. We refer to the former as all and to the second as low-high setting. For all settings, in the hyperparameters tuning stage and for the final hyperparameters choice, fifteen trainings with random weights initialization are performed and the best one in terms of testing error using the DNS Re_b values is kept. For additional insights of the final architectures, we refer to Appendix E.

6.3. **ROM results.** In this section, we compare the PODG SIMPLE and the PODNN results. For the sake of brevity, we only present the results obtained by choosing the reduced space generated by the all-POD. The same conclusions hold if the low-high approach is investigated. In the PODG SIMPLE method, we use a trivial initial condition for b and $a_i = 0$ for $i = 2, ..., r_u$ and a_1 such that the initial reduced velocity $\mathbf{u}_r^0 = a_1 \boldsymbol{\varphi}_1$ has streamwise average velocity equal to U_b . The PODG SIMPLE method is implemented using the ITHACA-FV library [42, 43].

Figures 11 and 12 compare u_x/U_b and I_s of the two ROM approaches with respect to the FOM reference both at $Re_b = 1600$ and $Re_b = 2900$. We immediately observe that the PODG SIMPLE approach gives unphysical solutions. In particular, it predicts negative streamwise velocities and the highest streamwise velocities near the wall and drastically overpredicts the secondary motion. In contrast, the PODNN model accurately predicts all flow features both qualitatively and quantitatively for both Reynolds numbers. The difficulty of the PODG SIMPLE algorithm to converge to the correct solution for turbulent flows has been already observed in [55], where the authors added snapshots of intermediate iterations of the FOM SIMPLE method to build the snapshots matrix. In this way, the reduced basis is able to drive at the intermediate iterations the ROM algorithm towards the correct solution. Clearly, this approach increases the memory storage requirements and the computational burden of the offline-stage. Because the PODNN method is able to correctly describe all the flow methodology, we decide to focus on this method and to better investigate possible issues mitigation for the PODG SIMPLE algorithm in future works.

Remark 3. The PODG SIMPLE results presented in this section have been obtained projecting the FOM system with the exact ν_t and \mathbf{t}^{\perp} fields to be consistent with the FOM procedure. We have also investigated the effect of projecting into the Navier-Stokes equations, thus neglecting the turbulent fields. We observed analogous results in terms of poor flow representation. We do not present them for the sake of conciseness.

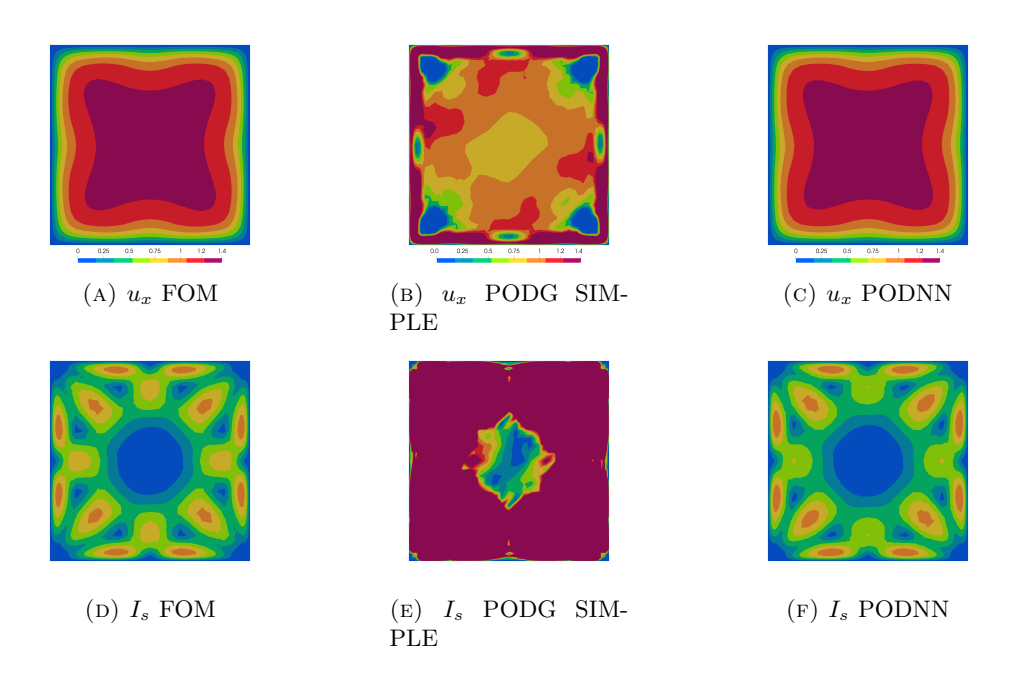


FIGURE 11. Comparison of u_x/U_b and I_s obtained with the FOM, the PODG SIMPLE and PODNN models at $Re_b = 1600$.

The PODNN strategy involves one neural network inference only at inference stage and, consequently, it is computationally cheap. Table 3 shows the average execution times for the LS $k-\varepsilon$ RANS model, for the ν_t -VBNN model, taking into account only the simulation time with inferred ν_t and t^{\perp} fields using as initial condition the LS $k-\varepsilon$ fields, and for the PODNN model. The average is performed over 110 simulations with $Re_b=1310,1330,\ldots,3490$. The speedup is defined as the ratio of the total time to run a FOM simulation, i.e., the sum of the first two columns of Table 3, divided by the PODNN inference time. From a FOM perspective, using the ν_t -VBNN increases the execution time by 18%. From a ROM perspective, the PODNN approach gives an average speedup of $O(10^5)$ with respect to FOM, thus justifying the PODNN choice.

6.4. The effect of training the PODNN on separate flow regimes. As for the ν_t -VBNN model at the FOM level, we investigate the effect of training the PODNN separately depending on the flow regime. To do that, we compute the reduced coefficients for the training using the low-POD or high-POD reduced basis, depending on the Re_b number. Then, two neural networks are trained, one for each flow regime. We denote the resulting model consisting of two trained networks as

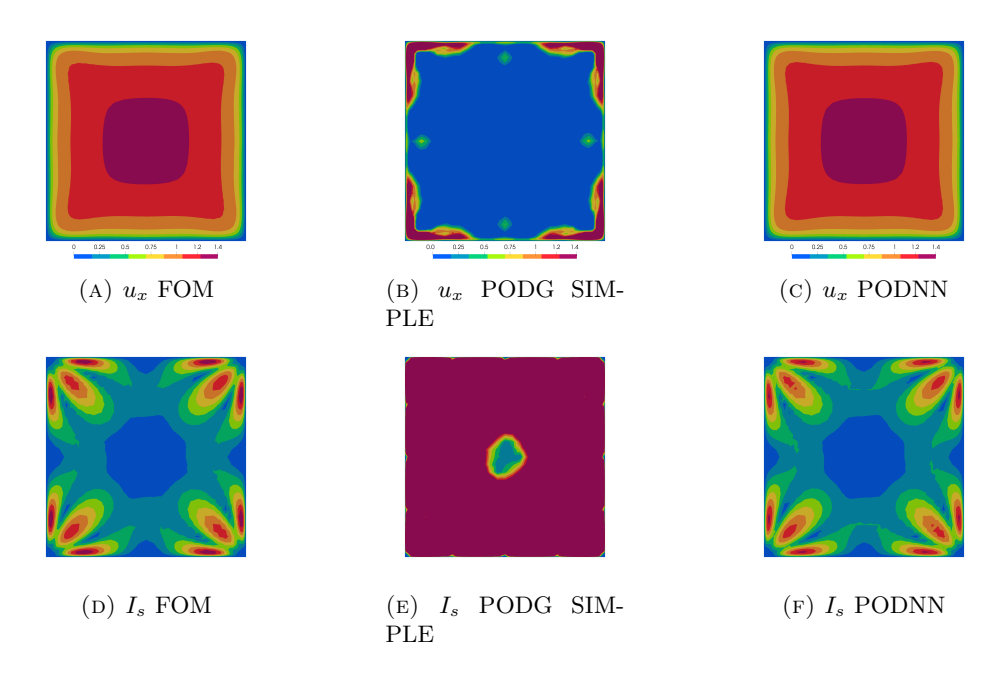


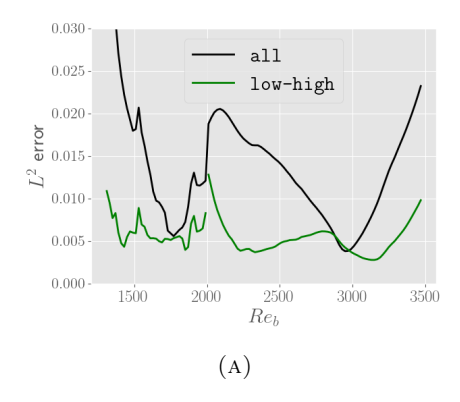
FIGURE 12. Comparison of u_x/U_b and I_s obtained with the FOM, the PODG SIMPLE and PODNN models at $Re_b = 2900$.

Table 3. Average time over 110 simulations for the $k-\varepsilon$ RANS model, the LS ν_t -VBNN enhanced RANS model (with LS $k-\varepsilon$ RANS results as initial condition) and for the PODNN. The speedup of the PODNN is computed using the sum of the first two columns.

$k - \varepsilon$ time [s]	ν_t -VBNN time $[s]$	PODNN time [s]	speedup
$1.38~\mathrm{e}2$	2.51 e1	7.72 e-4	2.12 e5

low-high. Analogously, we denote the PODNN model trained using all data as all. For the sake of simplicity, the same hyperparameters are selected for all networks. As before, fifteen trainings are performed for each neural network and the best one in terms of average testing error is selected. Figure 13a shows the average L^2 error across the fifteen trainings for both the all and the low-high predicted velocity fields. We point out that the error has a discontinuity at $Re_b = 2000$ even for the all model. This is due to using as FOM the low-high ν_t -VBNN model that uses two distinct models depending on the interval. From the Figure, it appears that using two neural networks, each of them focusing on a specific flow regime, extremely increases the accuracy. As a matter of fact, the maximum all error is greater than 3% while the higher error of the low-high model is smaller than 1.5%.

Finally, we also investigate the effect of training the two neural networks using two Re_b intervals that partially overlap. In particular, the low model is trained using data for $Re_b \leq 2200$ while the high model with data for $Re_b \geq 1800$. The



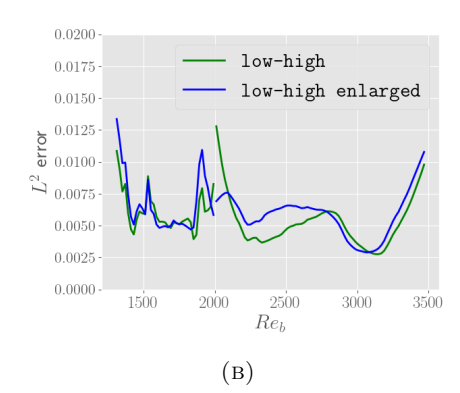


FIGURE 13. Comparison of the average relative L^2 errors for the PODNN inferred \boldsymbol{u} fields.

averaged error of this approach called low-high enlarged is shown in Figure 13b and compared to the low-high one. For $Re_b > 2000$, it appears that extending the training interval is beneficial to reduce the error peak at $Re_b \approx 2000$, while the error increases elsewhere but at a lower extent. Conversely, this approach does not significantly affect the results for $Re_b < 2000$. To conclude, the low-high enlarged model can be used for the $Re_b > 2000$ interval, aiming to make the error more uniform across the Re_b interval, while keeping the advantages of using separate training.

7. Conclusions and perspectives

In this work, we investigate the possibility of combining ML-based RANS closure models and ROM. In particular, the ν_t -VBNN model [1, 27] is used to close through two neural networks the RANS equations. Such a model is trained using DNS data to attain high accuracy while maintaining the computational cost of the RANS framework. Once properly trained, the ν_t -VBNN model is used to generate FOM simulations to retrieve a reduced space in which apply ROM methodologies. In this work, a non-intrusive ROM model, i.e., purely data-driven, called PODNN, and an intrusive one, i.e., projection-based, called PODG SIMPLE are tested. The former uses a neural network to approximate the map from the parameter-space to the reduced coefficients of the reduced solution. The latter mimics the SIMPLE iterative algorithm used at the FOM level to decouple velocity and pressure fields. These methodologies, both at the FOM and the ROM level, are tested in the flow in a square duct with varying bulk Reynolds number Re_b [34].

To schematically synthesize the results of the present work:

- at the FOM level, the ν_t -VBNN is trained to build an accurate model. In contrast with the common choice in literature, we train our model covering both the transitional regime and the fully turbulent one. In this way, we challenge our ML-based RANS model and investigate the effect of training specialization into the two distinct regimes;
- at the ROM level, we compare a non-intrusive model and an intrusive one. The former is well-suited to our setting while the latter provides inaccurate results. Also at the ROM level, we cover both the transitional regime and

the fully turbulent one, and investigate the effects of a training splitting scenario.

Many are the valuable extensions of this contribution. First, a deeper analysis on how to stabilize the PODG SIMPLE approach for the flow in a square duct and, in general, for turbulent flows is worth investigating. As a matter of fact, it is well known that intrusive approaches for convection dominated and turbulent flows can require ad-hoc and problem-dependent stabilization techniques [15, 40, 60]. Another line of research is represented by defining closure models at the ROM level to retrieve the ν_t and t^{\perp} reduced fields. Furthermore, it would be of great interest to investigate more complex flow phenomena and move to more sophisticated, possibly not based on a linear expansion at the ROM level, non-intrusive models for flows with high Kolmogorov n-width.

ACKNOWLEDGEMENTS

All authors are members of the Gruppo Nazionale Calcolo Scientifico-Istituto Nazionale di Alta Matematica (GNCS-INdAM). SB kindly acknowledges financial support by PNRR M4C2 project of CN00000013 National Centre for HPC, Big Data and Quantum Computing (HPC) CUP: E13C22000990001. DO acknowledges the support provided by the European Union-NextGenerationEU, in the framework of the iNEST-Interconnected Nord-Est Innovation Ecosystem (iNEST ECS00000043–CUP G93C22000610007) consortium. Moreover, this study was carried out within the "20227K44ME - Full and Reduced order modelling of coupled systems: focus on non-matching methods and automatic learning (FaReX)" project – funded by European Union – Next Generation EU within the PRIN 2022 program (D.D. 104 - 02/02/2022 Ministero dell'Università e della Ricerca).DO and MS thank the INdAM-GNCS Project "Metodi numerici efficienti per problemi accoppiati in sistemi complessi" (CUP E53C24001950001). MS thanks and the ECCOMAS EYIC Grant "CRAFT: Control and Reg-reduction in Applications for Flow Turbulence".

References

- [1] Berrone, S., and Oberto, D. An invariances-preserving vector basis neural network for the closure of Reynolds-averaged Navier–Stokes equations by the divergence of the Reynolds stress tensor. *Physics of Fluids 34*, 9 (2022).
- [2] Brener, B. P., Cruz, M. A., Thompson, R. L., and Anjos, R. P. Conditioning and accurate solutions of Reynolds average Navier—Stokes equations with data-driven turbulence closures. *Journal of Fluid Mechanics 915* (2021), A110.
- [3] Bruno, L., and Oberto, D. Effects of cell quality in grid boundary layer on the simulated flow around a square cylinder. *Computers & Fluids 238* (2022), 105351.
- [4] CRAFT, T., LAUNDER, B., AND SUGA, K. Development and application of a cubic eddyviscosity model of turbulence. *International Journal of Heat and Fluid Flow 17*, 2 (1996), 108–115.
- [5] CRUZ, M. A., THOMPSON, R. L., SAMPAIO, L. E., AND BACCHI, R. D. The use of the Reynolds force vector in a physics informed machine learning approach for predictive turbulence modeling. Computers & Fluids 192 (2019), 104258.
- [6] DE ZORDO-BANLIAT, M., DERGHAM, G., MERLE, X., AND CINNELLA, P. Space-dependent turbulence model aggregation using machine learning. *Journal of Computational Physics* 497 (2024), 112628.
- [7] FERGIZER, J. H., PERIC, M., AND STREET, R. L. Computational Method for Fluid Dynamic. Springer, 2020.
- [8] FONSECA, E. F., RANGEL, V. B., BRENER, B. P., CRUZ, M. A., AND THOMPSON, R. L. Preprocessing DNS data to improve statistical convergence and accuracy of mean velocity fields

- in invariant data-driven turbulence models. Theoretical and Computational Fluid Dynamics 36, 3 (2022), 435–463.
- [9] GOODFELLOW, I., BENGIO, Y., AND COURVILLE, A. Deep Learning. MIT Press, 2016. http://www.deeplearningbook.org.
- [10] HESTHAVEN, J., AND UBBIALI, S. Non-intrusive reduced order modeling of nonlinear problems using neural networks. *Journal of Computational Physics* 363 (2018), 55–78.
- [11] HESTHAVEN, J. S., ROZZA, G., AND STAMM, B. Certified Reduced Basis Methods for Parametrized Partial Differential Equations. Springer, 2015.
- [12] HIJAZI, S., STABILE, G., MOLA, A., AND ROZZA, G. Data-driven POD-Galerkin reduced order model for turbulent flows. *Journal of Computational Physics* 416 (2020), 109513.
- [13] INGIMARSON, S., REBHOLZ, L. G., AND ILIESCU, T. Full and reduced order model consistency of the nonlinearity discretization in incompressible flows. Computer Methods in Applied Mechanics and Engineering 401 (2022), 115620.
- [14] IVAGNES, A., STABILE, G., MOLA, A., ILIESCU, T., AND ROZZA, G. Hybrid data-driven closure strategies for reduced order modeling. Applied Mathematics and Computation 448 (2023), 127920.
- [15] IVAGNES, A., STRAZZULLO, M., GIRFOGLIO, M., ILIESCU, T., AND ROZZA, G. Data-driven optimization for the evolve-filter-relax regularization of convection-dominated flows. *Interna*tional Journal for Numerical Methods in Engineering 126, 9 (2025), e70042.
- [16] JASAK, H. Error analysis and estimation in the Finite Volume method with applications to fluid flows. PhD thesis, Imperial College, 1996.
- [17] JIANG, C., VINUESA, R., CHEN, R., MI, J., LAIMA, S., AND LI, H. An interpretable framework of data-driven turbulence modeling using deep neural networks. *Physics of Fluids* 33, 5 (2021), 055133.
- [18] Kingma, D. P., and Ba, J. Adam: A method for stochastic optimization.
- [19] LAUNDER, B., AND SHARMA, B. Application of the energy-dissipation model of turbulence to the calculation of flow near a spinning disc. Letters in Heat and Mass Transfer 1, 2 (1974), 131–137.
- [20] LING, J., KURZAWSKI, A., AND TEMPLETON, J. Reynolds averaged turbulence modelling using deep neural networks with embedded invariance. *Journal of Fluid Mechanics* 807 (2016), 155–166.
- [21] LING, J., AND TEMPLETON, J. Evaluation of machine learning algorithms for prediction of regions of high Reynolds averaged Navier Stokes uncertainty. *Physics of Fluids* 27, 8 (2015), 085103.
- [22] MCCONKEY, R., YEE, E., AND LIEN, F.-S. A curated dataset for data-driven turbulence modelling. Scientific Data 8, 1 (2021).
- [23] MCCONKEY, R., YEE, E., AND LIEN, F.-S. On the generalizability of machine-learningassisted anisotropy mappings for predictive turbulence modelling. *International Journal of Computational Fluid Dynamics* 36, 7 (2022), 555–577.
- [24] Menter, F. Zonal Two Equation k-w Turbulence Models For Aerodynamic Flows. 2012.
- [25] MOIN, P., AND KIM, J. Tackling turbulence with supercomputers. Scientific American 276, 1 (1997), 62–68.
- [26] MOUKALLED, F., MANGANI, L., AND DARWISH, M. The Finite Volume Method in Computational Fluid Dynamics: An Advanced Introduction with OpenFOAM® and Matlab. Springer International Publishing, 2016.
- [27] OBERTO, D. Improving the vector basis neural network for RANS equations using separate trainings. In *Numerical Mathematics and Advanced Applications ENUMATH 2023, Volume* 2 (Cham, 2025), A. Sequeira, A. Silvestre, S. S. Valtchev, and J. Janela, Eds., Springer Nature Switzerland, pp. 203–212.
- [28] OBERTO, D., FRANSOS, D., AND BERRONE, S. Using delayed detached eddy simulation to create datasets for data-driven turbulence modeling: A periodic hills with parameterized geometry case. Computers & Fluids 288 (2025), 106506.
- [29] OLIVER, T. A., AND MOSER, R. D. Bayesian uncertainty quantification applied to RANS turbulence models. *Journal of Physics: Conference Series* 318, 4 (2011), 042032.
- [30] OULGHELOU, M., CHERROUD, S., MERLE, X., AND CINNELLA, P. Machine-learning-assisted blending of data-driven turbulence models. Flow, Turbulence and Combustion (2025).

- [31] PASZKE, A., GROSS, S., CHINTALA, S., CHANAN, G., YANG, E., DEVITO, Z., LIN, Z., DES-MAISON, A., ANTIGA, L., AND LERER, A. Automatic differentiation in pytorch. In NIPS-W (2017).
- [32] PATANKAR, S., AND SPALDING, D. A calculation procedure for heat, mass and momentum transfer in three-dimensional parabolic flows. *International Journal of Heat and Mass Trans*fer 15, 10 (1972), 1787–1806.
- [33] PICHI, F., BALLARIN, F., ROZZA, G., AND HESTHAVEN, J. S. An artificial neural network approach to bifurcating phenomena in computational fluid dynamics. *Computers & Fluids* 254 (2023), 105813.
- [34] PINELLI, A., UHLMANN, M., SEKIMOTO, A., AND KAWAHARA, G. Reynolds number dependence of mean flow structure in square duct turbulence. *Journal of Fluid Mechanics* 644 (2010), 107–122.
- [35] PIROZZOLI, S., MODESTI, D., ORLANDI, P., AND GRASSO, F. Turbulence and secondary motions in square duct flow. *Journal of Fluid Mechanics* 840 (2018), 631–655.
- [36] Pope, S. B. Turbulent Flows. Cambridge University Press, 2000.
- [37] QUARTERONI, A., AND ROZZA, G. Reduced Order Methods for Modeling and Computational Reduction. Springer International Publishing, 2014.
- [38] REYNOLDS, O. IV. on the dynamical theory of incompressible viscous fluids and the determination of the criterion. Philos. Trans. R. Soc. Lond. A 186, 0 (1895), 123–164.
- [39] RINCÓN, M. J., AMARLOO, A., RECLARI, M., YANG, X. I., AND ABKAR, M. Progressive augmentation of Reynolds stress tensor models for secondary flow prediction by computational fluid dynamics driven surrogate optimisation. *International Journal of Heat and Fluid Flow* 104 (2023), 109242.
- [40] SIENA, P., GIRFOGLIO, M., QUAINI, A., AND ROZZA, G. Stabilized POD reduced order models for convection-dominated incompressible flows. *Computational and Applied Mathematics* 44, 7 (2025).
- [41] SPALART, P., AND ALLMARAS, S. A one-equation turbulence model for aerodynamic flows. In 30th Aerospace Sciences Meeting and Exhibit (1992), American Institute of Aeronautics and Astronautics.
- [42] STABILE, G., HIJAZI, S., MOLA, A., LORENZI, S., AND ROZZA, G. POD-Galerkin reduced order methods for CFD using Finite Volume Discretisation: vortex shedding around a circular cylinder. Communications in Applied and Industrial Mathematics 8, 1 ((2017)), 210–236.
- [43] STABILE, G., AND ROZZA, G. Finite volume POD-Galerkin stabilised reduced order methods for the parametrised incompressible Navier-Stokes equations. *Computers & Fluids* (2018).
- [44] STABILE, G., ZANCANARO, M., AND ROZZA, G. Efficient geometrical parametrization for finite-volume-based reduced order methods. *International Journal for Numerical Methods* in Engineering 121, 12 (2020), 2655–2682.
- [45] STRAZZULLO, M., BALLARIN, F., ILIESCU, T., AND REBOLLO, T. C. Variational multiscale evolve and filter strategies for convection-dominated flows. Computer Methods in Applied Mechanics and Engineering 438 (2025).
- [46] STRAZZULLO, M., GIRFOGLIO, M., BALLARIN, F., ILIESCU, T., AND ROZZA, G. Consistency of the full and reduced order models for evolve-filter-relax regularization of convectiondominated, marginally-resolved flows. *International Journal for Numerical Methods in En*gineering 123, 14 (2022), 3148–3178.
- [47] THOMPSON, R. L., SAMPAIO, L. E. B., DE BRAGANÇA ALVES, F. A., THAIS, L., AND MOM-PEAN, G. A methodology to evaluate statistical errors in DNS data of plane channel flows. Computers & Fluids 130 (2016), 1–7.
- [48] Wang, J.-X., Wu, J.-L., and Xiao, H. Physics-informed machine learning approach for reconstructing Reynolds stress modeling discrepancies based on DNS data. *Physical Review Fluids* 2, 3 (2017), 034603.
- [49] WELLER, H. G., TABOR, G., JASAK, H., AND FUREBY, C. A tensorial approach to computational continuum mechanics using object-oriented techniques. *Computers in Physics* 12, 6 (1998), 620.
- [50] WILCOX, D. Turbulence Modeling for CFD (Third Edition) (Hardcover). Dcw Industries, 2006.
- [51] WILCOX, D. C. Formulation of the $k-\omega$ turbulence model revisited. AIAA Journal 46, 11 (2008), 2823–2838.

- [52] Wu, J., Xiao, H., Sun, R., and Wang, Q. Reynolds-averaged Navier-Stokes equations with explicit data-driven Reynolds stress closure can be ill-conditioned. *Journal of Fluid Mechanics* 869 (2019), 553-586.
- [53] Wu, J.-L., Xiao, H., and Paterson, E. Physics-informed machine learning approach for augmenting turbulence models: A comprehensive framework. *Physical Review Fluids 3*, 7 (2018), 074602.
- [54] XIAO, H., WU, J.-L., LAIZET, S., AND DUAN, L. Flows over periodic hills of parameterized geometries: A dataset for data-driven turbulence modeling from direct simulations. *Computers & Fluids* 200 (2020), 104431.
- [55] ZANCANARO, M., HIJAZI, S., GIRFOGLIO, M., MOLA, A., STABILE, G., AND ROZZA, G. Chapter 8: Finite Volume-Based Reduced Order Models for Turbulent Flows. Society for Industrial and Applied Mathematics, 2022, pp. 165–202.
- [56] ZANCANARO, M., HIJAZI, S., MORELLI, U., STABILE, G., AND ROZZA, G. Chapter 7: Finite Volume-Based Reduced Order Models for Laminar Flows. Society for Industrial and Applied Mathematics, 2022, pp. 141–164.
- [57] ZANCANARO, M., MROSEK, M., STABILE, G., OTHMER, C., AND ROZZA, G. Hybrid neural network reduced order modelling for turbulent flows with geometric parameters. *Fluids* 6, 8 (2021), 296.
- [58] ZHENG, Q.-S. Theory of representations for tensor functions—a unified invariant approach to constitutive equations. Applied Mechanics Reviews 47, 11 (1994), 545–587.
- [59] ZOCCOLAN, F., STRAZZULLO, M., AND ROZZA, G. Stabilized weighted reduced order methods for parametrized advection-dominated optimal control problems governed by partial differential equations with random inputs. *Journal of Numerical Mathematics* (2024).
- [60] ZOCCOLAN, F., STRAZZULLO, M., AND ROZZA, G. A streamline upwind Petrov-Galerkin reduced order method for advection-dominated partial differential equations under optimal control. Computational Methods in Applied Mathematics 25, 1 (2025), 237 260.

APPENDIX A. INVARIANTS AND VECTOR BASIS OF THE ν_t -VBNN MODEL In [27], the following assumption is made:

$$\widetilde{\boldsymbol{t}}^{\perp} = \widetilde{\boldsymbol{t}}^{\perp}(\mathbf{s}, \mathbf{w}, \widetilde{\nabla \cdot \mathbf{S}}, \widetilde{\nabla k}, Re_d),$$

where $\mathbf{s} = \frac{k}{\varepsilon} \mathbf{S}$, $\mathbf{w} = \frac{k}{\varepsilon} \mathbf{W}$, $\widetilde{\nabla \cdot \mathbf{S}} = \frac{k^{5/2}}{\varepsilon^2} \nabla \cdot \mathbf{S}$ and $\widetilde{\nabla k} = \frac{k^{1/2}}{\varepsilon} \nabla k$ are the dimensionless counterparts of \mathbf{S} , \mathbf{W} , $\nabla \cdot \mathbf{S}$ and ∇k , respectively. Finally, $Re_d = \min(\frac{\sqrt{k}d}{50\nu}, 2)$ is the wall-distance based Reynolds number, where d is the wall distance.

With this assumption, we obtain (5b) [58], where the vector basis reads

$$\begin{split} &\mathbf{v}_1 = \widetilde{\nabla \cdot \mathbf{S}}, \quad \mathbf{v}_2 = \mathbf{s} \ \widetilde{\nabla \cdot \mathbf{S}}, \quad \mathbf{v}_3 = \mathbf{s}^2 \ \widetilde{\nabla \cdot \mathbf{S}}, \\ &\mathbf{v}_4 = \mathbf{w} \ \widetilde{\nabla \cdot \mathbf{S}}, \quad \mathbf{v}_5 = \mathbf{w}^2 \ \widetilde{\nabla \cdot \mathbf{S}}, \quad \mathbf{v}_6 = (\mathbf{s}\mathbf{w} + \mathbf{w}\mathbf{s}) \ \widetilde{\nabla \cdot \mathbf{S}}, \\ &\mathbf{v}_7 = \widetilde{\nabla k}, \quad \mathbf{v}_8 = \mathbf{s} \ \widetilde{\nabla k}, \quad \mathbf{v}_9 = \mathbf{s}^2 \ \widetilde{\nabla k}, \\ &\mathbf{v}_{10} = \mathbf{w} \ \widetilde{\nabla k}, \quad \mathbf{v}_{11} = \mathbf{w}^2 \ \widetilde{\nabla k}, \quad \mathbf{v}_{12} = (\mathbf{s}\mathbf{w} + \mathbf{w}\mathbf{s}) \ \widetilde{\nabla k}, \end{split}$$

while the invariants are

$$\lambda_{1} = (\widetilde{\nabla \cdot \mathbf{S}})^{T} (\widetilde{\nabla \cdot \mathbf{S}}), \quad \lambda_{2} = \operatorname{tr}(\mathbf{s}^{2}), \quad \lambda_{3} = \operatorname{tr}(\mathbf{s}^{3}), \quad \lambda_{4} = \operatorname{tr}(\mathbf{w}^{2}),$$

$$\lambda_{5} = \operatorname{tr}(\mathbf{s}\mathbf{w}^{2}), \quad \lambda_{6} = \operatorname{tr}(\mathbf{s}^{2}\mathbf{w}^{2}), \quad \lambda_{7} = \operatorname{tr}(\mathbf{s}^{2}\mathbf{w}^{2}\mathbf{s}\mathbf{w}), \quad \lambda_{8} = (\widetilde{\nabla \cdot \mathbf{S}})^{T}\mathbf{s}(\widetilde{\nabla \cdot \mathbf{S}}),$$

$$\lambda_{9} = (\widetilde{\nabla \cdot \mathbf{S}})^{T}\mathbf{s}^{2}(\widetilde{\nabla \cdot \mathbf{S}}), \quad \lambda_{10} = (\widetilde{\nabla \cdot \mathbf{S}})^{T}\mathbf{w}^{2}(\widetilde{\nabla \cdot \mathbf{S}}), \quad \lambda_{11} = (\widetilde{\nabla \cdot \mathbf{S}})^{T}\mathbf{s}\mathbf{w}(\widetilde{\nabla \cdot \mathbf{S}}),$$

$$\lambda_{12} = (\widetilde{\nabla \cdot \mathbf{S}})^{T}\mathbf{s}^{2}\mathbf{w}(\widetilde{\nabla \cdot \mathbf{S}}), \quad \lambda_{13} = (\widetilde{\nabla \cdot \mathbf{S}})^{T}\mathbf{w}\mathbf{s}\mathbf{w}^{2}(\widetilde{\nabla \cdot \mathbf{S}}),$$

$$\lambda_{14} = (\widetilde{\nabla k})^{T}(\widetilde{\nabla k}), \quad \lambda_{15} = (\widetilde{\nabla k})^{T}\mathbf{s}(\widetilde{\nabla k}), \quad \lambda_{16} = (\widetilde{\nabla k})^{T}\mathbf{s}^{2}(\widetilde{\nabla k}),$$

$$\lambda_{17} = (\widetilde{\nabla k})^{T}\mathbf{w}^{2}(\widetilde{\nabla k}), \quad \lambda_{18} = (\widetilde{\nabla k})^{T}\widetilde{\nabla \cdot \mathbf{S}}, \quad \lambda_{19} = (\widetilde{\nabla k})^{T}\mathbf{s}\mathbf{w}(\widetilde{\nabla k}),$$

$$\lambda_{20} = (\widetilde{\nabla k})^{T}\mathbf{s}^{2}\mathbf{w}(\widetilde{\nabla k}), \quad \lambda_{21} = (\widetilde{\nabla k})^{T}\mathbf{w}\mathbf{s}\mathbf{w}^{2}(\widetilde{\nabla k}), \quad \lambda_{22} = (\widetilde{\nabla k})^{T}\mathbf{s}\mathbf{w}(\widetilde{\nabla \cdot \mathbf{S}}),$$

$$\lambda_{23} = (\widetilde{\nabla k})^{T}\mathbf{s}^{2}\mathbf{w}(\widetilde{\nabla \cdot \mathbf{S}}), \quad \lambda_{24} = (\widetilde{\nabla k})^{T}\mathbf{w}(\widetilde{\nabla \cdot \mathbf{S}}),$$

$$\lambda_{25} = (\widetilde{\nabla k})^{T}\mathbf{w}\mathbf{s}\mathbf{w}^{2}(\widetilde{\nabla \cdot \mathbf{S}}), \quad \lambda_{26} = (\widetilde{\nabla k})^{T}(\mathbf{s}\mathbf{w} + \mathbf{w}\mathbf{s})(\widetilde{\nabla \cdot \mathbf{S}}),$$

$$\lambda_{27} = Re_{d}.$$

The first twenty-six invariants come from the dependencies on $\mathbf{s}, \mathbf{w}, \nabla \cdot \mathbf{S}, \nabla k$. We observe that the invariant $\mathrm{tr}(\mathbf{s})$ is neglected because of the incompressibility constraint.

Finally, because $\tilde{\nu}_t$ is a scalar field, we directly use (5a) without involving any linear expansion.

APPENDIX B. THE ROLE OF u_t AND \mathbf{t}^{\perp} IN THE SECONDARY MOTION PREDICTION

In Figure 14, we compare the ν_t field of the DNS simulation interpolated on the RANS mesh and the one predicted by the standard LS $k-\varepsilon$ for $Re_b=2900$. The maxima loci of the DNS are not situated at the center of the section, whereas the LS $k-\varepsilon$ field monotonically increases moving closer to the section center. Additionally, the LS $k-\varepsilon$ field assumes higher values with respect to the DNS ν_t .

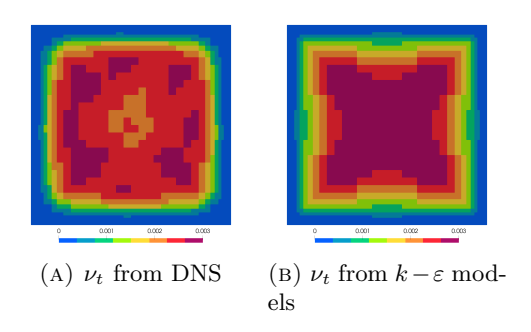


FIGURE 14. Comparison between the DNS ν_t (left) and the one predicted by the $k - \varepsilon$ model (right) for $Re_b = 2900$.

To understand how the ν_t discrepancy affects the predicted secondary motion, in Figure 15 we show I_s at $Re_b = 2900$ when using both ν_t and \mathbf{t}^{\perp} from DNS, the DNS ν_t only, the LS $k - \varepsilon \nu_t$ and, finally, the LS $k - \varepsilon \nu_t$ and the DNS $\tilde{\mathbf{t}}^{\perp}$. All the DNS fields have been interpolated on the RANS mesh. We deduce that the

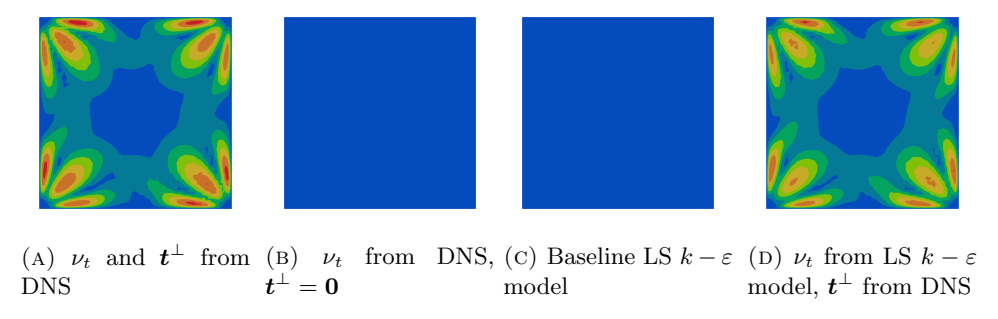


FIGURE 15. I_s when fixing ν_t and/or \mathbf{t}^{\perp} at $Re_b = 2900$. The same color scale of Figure 2 has been used for all figures.

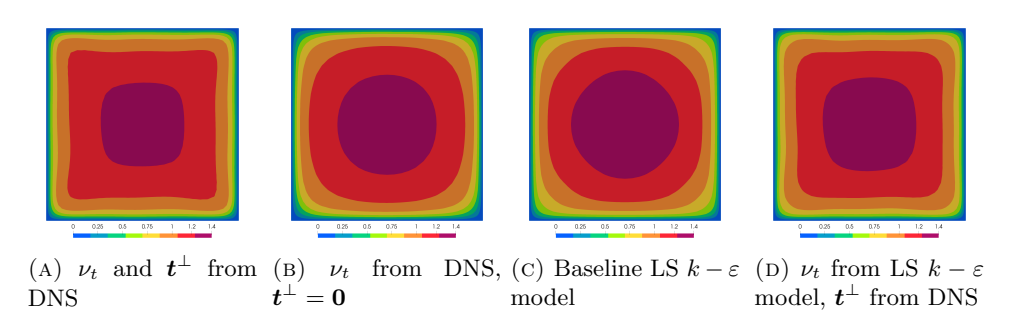


FIGURE 16. u_x/U_b when fixing ν_t and/or \mathbf{t}^{\perp} from DNS at $Re_b = 2900$.

secondary motion is correctly predicted only when including the t^{\perp} term in the RANS equations, while the accuracy of ν_t only slightly affects its magnitude. This behavior is expected: standard linear models, that do not consider any t^{\perp} term, systematically do not predict secondary motion.

An accurate secondary motion prediction is important to correctly describe the streamwise velocity. In particular, Figure 16 displays the corresponding predicted u_x/U_b fields. When secondary motion is predicted, i.e., Figures 16a and 16d, the contour lines of u_x/U_b have a square-like shape, while such contour lines have a circle-like shape when secondary motion is not predicted. This behavior is again expected: the secondary motion transports flow from the central region, with higher u_x/U_b , toward the corners, thus increasing the streamwise velocity along the diagonals.

Appendix C. The regularization role for the ν_t -VBNN model

It is well established in the ML community that the regularization factor plays a key role in the neural networks' prediction capability: a too low value can lead to overfitting, while a too high value can lead to underfitting [9]. Despite its importance, to the best of the authors' knowledge, no particular attention to this factor has been extensively commented on in the data-driven turbulence community when dealing with the duct flow case. To have a quantitative analysis on its relevance,

we select for both $\lambda_{\tilde{\nu}_t}$ and $\lambda_{\tilde{t}^{\perp}}$ the values $\{0, 10^{-5}, 10^{-4}, 10^{-3}\}$ and compute the Mean Squared Error (MSE) for the predicted $\tilde{\nu}_t$ and \tilde{t}^{\perp} with respect to DNS fields for each Re_b . Moreover, for each setting, we compute the average MSE across the fifteen performed trainings and compute the standard deviation (std). Figure 17 depicts these quantities with respect to Re_b in terms of the prediction of $\tilde{\nu}_t$.

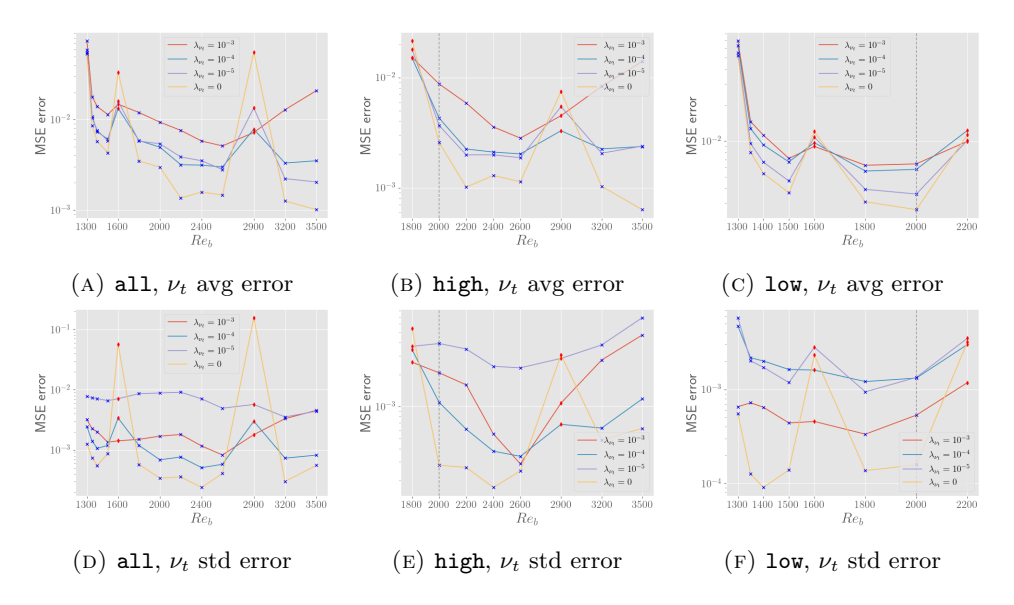


FIGURE 17. Comparison of average and std MSE with respect to Re_b for the $\tilde{\nu}_t$ prediction with different values of $\lambda_{\tilde{\nu}_t}$.

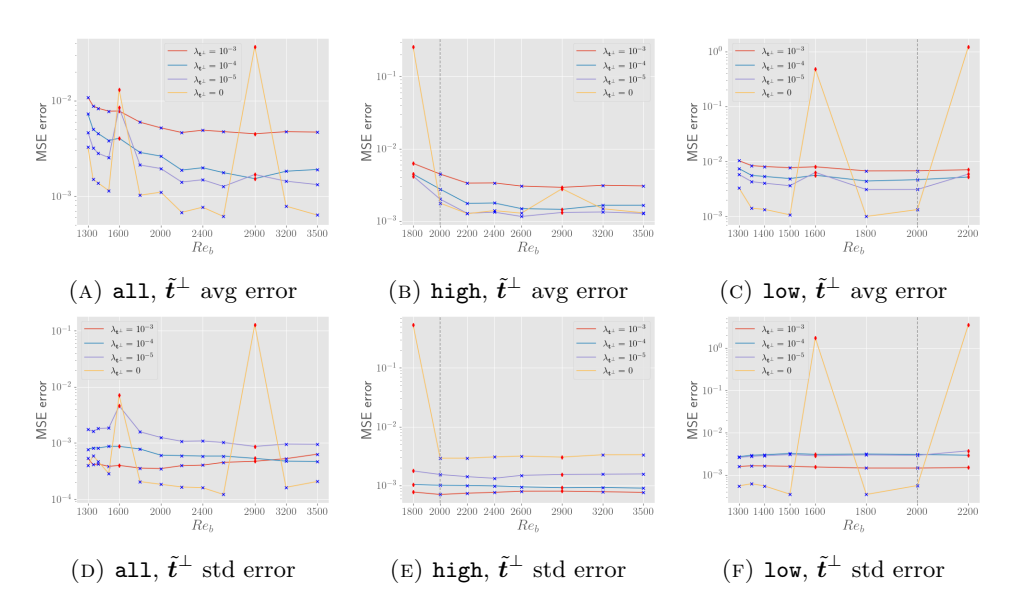


FIGURE 18. Comparison of average and std MSE with respect to to Re_b for the \tilde{t}^{\perp} prediction with different values of $\lambda_{\tilde{t}^{\perp}}$.

As expected, the lower $\lambda_{\tilde{\nu}_t}$, the lower the average error and the standard deviation when predicting for training Re_b values. However, a lower training error does not necessarily translate to a lower test error. As a matter of fact, the larger testing errors are always obtained when no regularization is considered during the training. Furthermore, scarce regularization increases the testing error variability, too, and makes the testing ability of the single trained network less reliable. The same analysis is performed for the $\lambda_{\tilde{t}^{\perp}}$ effect on the inferred \tilde{t}^{\perp} field. Figure 18 depicts the mean and standard deviation of the MSE. Similar conclusions can be drawn. To generate the ν_t -VBNN enhanced simulations, for each Re_b interval choice, we first select either $\lambda_{\tilde{\nu}_t}$ or $\lambda_{\tilde{t}^{\perp}}$ as the one with lowest average testing error. Then, among the fifteen networks trained with the selected regularization factors, we pick the best neural network in terms of testing error.

Appendix D. ν_t -VBNN hyperparameters

The hyperparameters for both the $\tilde{\nu}_t$ and \tilde{t}^{\perp} models are synthesized in Table 4, where n_inp denotes the number of inputs, n_out the number of outputs, n_hid the number of hidden layers, n_nodes the number of nodes per hidden layer and 1r the starting learning rate. Their values are consistent with the literature [1, 20, 28]. Except for the regularization factor, whose values are deeply investigated in Section 5 and Appendix C, all the hyperparameters are the same in all, low, and high settings. All networks are optimized using the Adam [18] algorithm, using a starting learning rate that is decreased during the training in case of stagnation of the validation loss. Mini-batching is performed with batch size equal to sixty-four.

Table 4. Hyperparameters for the ν_t -VBNN neural networks.

field	$n_{-}inp$	n_out	n_hid	n_nodes	lr
$ ilde{ u}_t$	27	1	8	30	5e-3
$ec{m{t}}^{\perp}$	27	12	8	30	5e-3

APPENDIX E. PODNN HYPERPARAMETERS

Table 5 shows the hyperparameters of the PODNN. The number of outputs depend on the number of predicted reduced coefficients and, consequently, it changes in the all, low and high settings. The reported hyperparameter values have been selected after a trial-and-error stage. The networks are trained using the Adam algorithm with a scheduled learning rate that decreases during the training. Because of the limited amount of data, the training is carried out for a maximum of $1.5 \cdot 10^4$ epochs, depending on whether the validation loss function stagnates before or not.

Table 5. Hyperparameters for the PODNN model. The same notation of Table 4 is used. Additionally, λ denotes the regularization factor.

field	$n_{-}inp$	n_out	n_hid	n_nodes	lr	λ
a	1	$\{13, 14, 22\}$	4	50	1e-3	1e-3